Frictional and Lithological Controls on Shallow Slow Slip at the Northern Hikurangi Margin

Srisharan Shreedharan[1+*], Matt Ikari[3], Clay Wood[1], Demian Saffer[4], Laura Wallace[4,5], Chris Marone[1,2]

[1]Dept. of Geosciences, Pennsylvania State University, University Park, PA 16802 USA

[2]Dipartimento di Scienze della Terra, La Sapienza Università di Roma, Italy

[3]MARUM Center for Marine Environmental Sciences and Faculty of Geosciences, University of Bremen, Bremen, Germany

[4]University of Texas Institute for Geophysics and Dept. of Geological Sciences, University of Texas, Austin, TX, USA

[5]GNS Science, Lower Hutt 5011, New Zealand

[+]Now at University of Texas Institute for Geophysics, Austin, TX, USA

***Corresponding author: srisharan@utexas.edu**

Abstract:

Slow slip events (SSEs) have been identified at subduction zones globally as an important link in the continuum between elastodynamic ruptures and stable creep. The northern Hikurangi margin is home to shallow SSEs which propagate to within 2 km of the seafloor and possibly to the trench, providing insights into the physical conditions conducive to SSE behavior. We report on a suite of friction experiments performed on protolith material entering the SSE source region at the Hikurangi margin, collected during the International Ocean Discovery Program Expedition 375. We performed velocity stepping and slide-hold-slide experiments over a range of fault slip rates, from plate rate (5 cm/yr) to ~1 mm/s and quantified the frictional velocity dependence and healing rates for a range of lithologies at different stresses. The friction velocity dependence (a-b) and critical slip distance Dc increase with fault slip rate in our experiments. We observe a transition from velocity weakening to strengthening at slip rates of ~0.3 μm/s. This velocity dependence of Dc could be due to a combination of dilatant strengthening and a widening of the active shear zone at higher slip rates. We document low healing rates in the clay-rich volcaniclastic conglomerates, which lie above the incoming plate basement at least locally, and relatively higher healing rates in the chalk lithology. Finally, our experimental constraints on healing rates in different input lithologies extrapolated to timescales of 1-10 years are consistent with the geodetically-inferred low stress drops and healing rates characteristic of the Hikurangi SSEs.

Keywords:

Slow earthquakes, Hikurangi, Friction, Slow slip

Key points:

- We quantify frictional stability and healing behavior of input material to the subduction plate interface at the northern Hikurangi margin
- Increasing frictional stability and critical slip distance with velocity may be key mechanisms responsible for shallow slow slip
- Velocity dependence of critical slip distance may be from a combination of dilatant strengthening and distributed slip at higher slip rates

1. Introduction:

Slow slip events (SSEs), lasting for days to months, have been widely recognized as an important part of the continuum bridging fast, elastodynamic ruptures and stable fault creep at plate boundaries globally (*Ide et al., 2007; Peng and Gomberg, 2010; Bürgmann, 2018*). These types of slip modes are particularly important because of the role they play in the seismic cycle and the accommodation of plate motion, and because of the clues they provide about plate interface rheology. In some cases, SSEs are thought to trigger ordinary fast earthquakes by loading adjacent fault patches (*Kato et al., 2012; Meng et al., 2015*). In other cases, SSEs have been triggered (*Araki et al., 2017; Wallace et al., 2017*) or arrested (*Wallace et al., 2014*) by nearby earthquakes. Thus, the precise role played by SSEs in the overall earthquake cycle is unclear. Moreover, many SSEs at convergent margins globally have been documented at the downdip limit of the seismogenic zone, i.e., at depths of 30 – 40 km (*Schwartz and Rokosky, 2007*), which makes it impossible to directly sample and study the frictional behavior of the active SSE source rocks.

The northern Hikurangi margin, offshore New Zealand, is an important example of shallow and accessible SSEs. These faults host robustly documented, quasi-periodic shallow SSEs (*Wallace, 2020*) that rupture close to the trench (*Wallace et al., 2016*) and have recurrence intervals of 12-18 months. Additionally, the source region of these SSEs has hosted tsunami earthquakes which may have ruptured to the trench (*Bell et al., 2014*) and is hypothesized to have significant pore fluid overpressure (*Bell et al., 2010; Bassett et al., 2014; Ellis et al., 2015*). Thus, it is important to constrain the frictional behavior of the source material to better understand the rock properties and processes that govern fault slip behavior, and ultimately the future risk of earthquake and tsunami generation.

Numerous studies have been undertaken in the laboratory to constrain the frictional behavior of natural fault zones (*e.g., Ikari et al., 2009; Ikari & Saffer, 2011; Carpenter et al., 2011; Carpenter et al., 2016; Ikari et al., 2020a*) and subduction inputs (e.g., *Kurzawski et al., 2016; Rabinowitz et al., 2018*). Specifically, of paramount importance are the frictional strength and the sliding stability of sheared faults. The latter quantity is usually defined within the framework of rate and state friction or RSF (*Marone, 1998*), which describes a set of constitutive equations motivated by laboratory experiments (*Dieterich, 1978, 1979; Ruina, 1983*). Broadly, laboratory observations of sliding friction can inform us about whether a fault will slide stably, resulting in aseismic creep, or unstably, giving rise to a range of slip modes including SSEs and fast dynamic earthquakes. Within this framework, SSEs arise naturally as a bridge between aseismic creep and elastodynamic ruptures based on an interaction between the fault zone elastic loading stiffness and a critical fault stiffness (*Gu et al., 1984; Leeman et al., 2016, 2018; Scuderi et al., 2017; Im et al., 2020*).

Recently, the International Ocean Discovery Program (IODP) Expeditions 372 and 375 sailed to the Hikurangi margin and sampled materials on the incoming Pacific Plate prior to subduction into the SSE region (*Barnes et al., 2019*). This provides an opportunity to sample and quantify the frictional behavior of materials likely playing an important role in hosting shallow SSEs. In particular, two distinct lithologies (chalks and phyllosilicate-rich volcaniclastic conglomerates) are abundant and likely represent a significant portion of the materials being subducted to the SSE source region based on tracing the seismic stratigraphy from the drill sites to the shallow subduction thrust (*Barnes et al., 2020*). Here, we present results from laboratory friction experiments designed to measure the frictional strength, sliding stability and healing behavior of these materials, at stresses and pore fluid pressures appropriate for conditions in the

shallow SSE source area. We present results over a range of fault slip rates, from plate tectonic rates, i.e., 5 cm/yr (*Ikari et al., 2015*), to slip rates of 1 mm/s, which far exceed the peak slip rates of the shallow SSEs in the study region.

2. The Hikurangi SSEs and IODP Expeditions 372/375

The Hikurangi subduction margin accommodates westward subduction of the Pacific plate beneath the Australian plate (Figure 1a) at a rate of ~2-6 cm/yr (*Wallace et al., 2004*). A range of SSEs, with significant along-strike variations, have been documented in this region (*Wallace, 2020* and refs. therein). In particular, the northern Hikurangi SSEs are shallower (depths <15 km), marked by shorter recurrence intervals (12-18 months) and durations (2-3 weeks) (*Wallace and Beavan, 2010*), and have been documented to propagate very close to the trench (*Wallace et al., 2016*). In contrast, the deeper (25-50 km depth) SSEs at the southern Hikurangi margin are marked by longer durations (3 – 24 months) and recurrence intervals of 4-5 years (*Wallace and Beavan, 2010; Bartlow et al., 2014*). Furthermore, the source region of the northern Hikurangi shallow SSEs is interpreted to be lithologically and geometrically heterogeneous (*Barnes et al., 2020*). For example, reflection seismic surveys (Figure 1b) show that the SSE source region is broadly coincident with high reflectivity zones (*Bell et al., 2010*) inferred to be regions of high pore fluid pressure and seamount subduction (*Bell et al., 2014; Barker et al., 2018; Todd et al., 2018*). Thus, these heterogeneities have been thought to play an important role in the nucleation of shallow SSEs and the interplay between SSEs and tsunami earthquakes. However, the physical processes surrounding the origins of these diverse SSE behaviors in this region remain poorly resolved, in part, because it is not easy to directly sample the source rocks.

IODP Expeditions 372 and 375, which sailed in late 2017 and early 2018, drilled at four sites to sample the upper plate, a splay fault (near the deformation front), and the sedimentary sequence on the incoming plate (Figure 1b) at the northern Hikurangi margin, offshore Gisborne, New Zealand (*Wallace et al., 2019*). Based on reflection seismic surveys and seismic correlations with core and logging data, key lithologies involved in the source region of the shallow SSEs have been identified as lying below 510 meters below seafloor (mbsf) at site U1520 (*Barnes et al., 2020*). Specifically, marls and chalk were found at 510-849 mbsf, and the lower portion of the sediment package (below 849 mbsf) consists of a volcaniclastic facies (Figure 2). The latter material contains basalt clasts, a clay-rich (primarily saponite) altered matrix and zeolite cementation and, for a few tens of meters, carbonate-rich cementation (Figure 2; *Barnes et al., 2019; Underwood, 2020*). Data from seismic reflection surveys (e.g., *Bell et al., 2014)* and regional drilling (*Barnes et al., 2020*) point to a plate interface which is likely patchy due to the heterogeneous incoming protolith containing regionally variable thicknesses of the carbonate and volcaniclastic sediments.

While clay- (and particularly smectite) rich sediments have been documented as being weak with a tendency for velocity-strengthening frictional behavior (e.g., *Saffer and Marone, 2003; Ikari et al., 2009; Ikari & Saffer, 2011; Ujiie et al., 2013*), carbonate-rich sediments are usually significantly stronger and can exhibit velocity weakening behavior especially at elevated temperatures (*Ikari et al*., 2013; *Tesei et al., 2014; Kurzawski et al., 2016*). Field, modeling and experimental studies (eg. *Ando et al., 2010; Nakata et al., 2011; Skarbek et al., 2012; Boulton et al., 2019*) have reported that geologic and lithological heterogeneities, i.e., mixtures of velocity weakening and strengthening sediments along plate interfaces may offer one explanation for the generation of SSEs. Previous studies reporting the frictional behavior of inputs to the Hikurangi

141 margin (*Raboniwitz et al., 2018; Boulton et al., 2019; Ikari et al., 2020a*) focused on shallower
142 sediments (200 – 450 mbsf) farther from the trench, from Ocean Drilling Program (ODP) Site
143 1124, which are compositionally similar to the marls (510 – 780 mbsf) at IODP Site U1520
144 (Figure 2). Here, we present results from friction experiments conducted on a larger range of
145 lithologies, and over a wider range of shearing rates and pore pressure conditions.
146
147 **3. Methods**
148 *3.1.Double-direct shear experiments (0.3 - 1000 μm/s)*
149 Biaxial experiments were conducted in a true-triaxial pressure vessel in a double direct-shear
150 (DDS) configuration in the Penn State Rock and Sediment Mechanics Laboratory (e.g.,
151 *Samuelson et al., 2009*). In this configuration, servo-controlled horizontal and vertical pistons
152 directly apply normal (σ) and shear stresses (τ) respectively to two gouge layers sandwiched
153 between three steel blocks (Figure 3a). Confining (P_c) and pore fluid pressures (inflow - P_{pA} and
154 outflow - P_{pB}) are independently servo-controlled via pressure intensifiers. Normal stress is
155 applied on the gouge layers (30 cm^2 nominal contact area) as a load boundary condition. Shear is
156 applied on the longer central forcing block through a prescribed loading/shearing rate, thus
157 deforming the sandwiched gouge layers. Grooves in sintered frits ensure that deformation occurs
158 within the gouge layers rather than localizing at the steel-gouge interface (Figure 3a) and
159 provides spatially-uniform fluid access to the fault zone. A confining pressure (oil-based) is
160 applied to achieve a true triaxial stress state. Rubber jackets surrounding the DDS assembly
161 ensure that the pore fluids in the sample remain isolated from the oil-based confining pressure. In
162 experiments where pore pressure is applied, the gouge layers are initially saturated by applying a
163 constant pressure to the pore fluid (de-ionized water) at the inflow end, and the outflow end is

connected to a vacuum pump. This ensures that the pore spaces are completely filled with the pore fluid. In our experiments, a constant pore pressure was applied on both the inflow and outflow sides during shear, keeping the sample under a drained boundary condition. While a temporarily undrained condition is possible internally in the gouge layers, past studies (*Ikari et al., 2009*) have demonstrated that significant pore pressure transients do not develop in our configuration. Previous studies have quantified that the rubber jackets have negligible strength (*Samuelson et al., 2009; Carpenter et al., 2016)*.

Normal and shear loads are measured using strain gauge load cells with a resolution of 0.1 kN. Fault normal and shear displacements are measured using direct-current linear variable differential transformers (DC-LVDTs). Confining pressure and associated volumetric changes are measured using a pressure transducer and a DC-LVDT affixed to the P_c intensifier. In the case of pore pressures, the pressure transducers are located close to the sample in order to minimize sensing volume and thus measure any small variations, whereas the displacement transducers (for measuring volumetric changes) are fixed to the P_{pA} and P_{pB} intensifiers. All pressure transducers have a measurement resolution of 7 kPa. Mechanical data are acquired continuously at 10 kHz and averaged to 100-1000 Hz in real-time for storage. All experiments were conducted at an effective normal stress (σ_{eff}) of 25 MPa, over a range of pore pressures and slip rates, from sub-slow slip rates of 0.3 μm/s (~1-3 cm/day) to 1000 μm/s. Table 1 contains the list of experiments and associated boundary conditions.

Input material sampled at four depth intervals (Figure 2) from Site U1520 were reconstituted and dried in an oven in vacuum at 40°C for 48 hours. Subsequently, the dry rocks were crushed, ground and sieved to a particle size of <125 μm. Gouge layers were constructed with a measured mass of material to ensure reproducibility and to a thickness of 5 mm width in a levelling jig (dry

187 and under atmospheric pressure conditions). Layer thickness was measured prior to load
188 application and at multiple points after the normal stress was applied, in order to calculate shear
189 strains. Deionized water (DI) was used to saturate the samples since the drying process
190 precipitates dissolved salts from the seawater into the sample. Thus, during saturation, we expect
191 the salts to dissolve into the DI water bringing the brine concentration and chemistry back to
192 levels that may closely resemble in-situ brine concentration.

193 Each experiment in the biaxial configuration consisted of a similar loading and shearing
194 protocol. We conducted 1-2 unload/reload cycles during the first 5 mm of shear (Figure 4) to
195 accelerate the development of a steady-state frictional behavior (*Saffer et al*., 2001; *Frye and*
196 *Marone, 2002; Mair and Marone, 1999*). We followed this with a sequence of velocity steps (0.3
197 – 1000 μm/s) and slide-hold-slide experiments (1 – 3000 s hold times) over a displacement range
198 of up to 25 mm (Figure 4).

199

200 *3.2.Single-direct shear experiments (10^{-3} - 1 μm/s)*

201 Low-velocity experiments were performed in a Giesa RS5 direct shear apparatus (Figure 3b)
202 to explore the frictional behavior of the U1520 input material over a range of slip rates from
203 plate-rate (1.6 μm/s, or 5 cm/yr) to slow-slip rates (0.5 μm/s, or 4.3 cm/day). In this experimental
204 configuration, disaggregated gouge was mixed with DI water to create a water-saturated paste
205 and placed in a sample cell (*Ikari et al., 2015*). The samples were sandwiched between porous
206 steel frits at room temperature and DI water saturated conditions. The normal stress was applied
207 vertically by vertical ram acting on a fixed top plate and the shear/loading rate was imposed by
208 translating the base plate (Figure 3b). This forced shear to localize along a narrow zone (up to
209 ~100s of μm thickness) as the two halves of the sample slide past each-other. Shear

displacements were measured at two locations – one referenced to a horizontal, shear load cell (with resolution 0.3 kPa) measured the imposed shear displacement (or load point displacement) and another referenced to the sample measured the slip accommodated by the sample itself. The sample freely communicates with the pore fluid reservoir, and is allowed to drain to the atmosphere in order to dissipate local pore pressure development. On application of the normal load (25 MPa), the sample was allowed to consolidate and drain to the atmosphere for at least ~18 hours, until a steady state sample thickness was achieved, prior to shear. Thus, by the nature of the experimental design, pore pressures were not measured, but the sample was assumed to be under drained, zero pore pressure conditions before shearing. Additionally, because the strain rates in this configuration are extremely low, we do not expect significant excess pore pressures to develop locally in the sample.

Samples were sheared at a run-in velocity of 10 μm/s for ~4-5 mm until a steady-state friction coefficient was achieved. Subsequently, velocity step experiments were conducted over the range of 1.6 nm/s to 0.5 μm/s.

3.3.Estimation of RSF parameters

In all experiments, the coefficient of friction (or simply referred to as friction), μ, is defined as the ratio of shear stress, τ, to effective normal stress, σ_{eff}.

$$\mu = \frac{\tau}{\sigma_{eff}} \quad (1)$$

In Eq. (1), σ_{eff} is the combined effect of the applied normal stress, σ_N, the net confining pressure acting normal to the gouge layers, and the applied pore pressure, P_p, and can be represented as

$$\sigma_{eff} = (\sigma_N + 0.629P_c) - P_p \quad (2)$$

Within the framework of RSF, the velocity dependence of friction can be described as follows:

$$\mu = \mu_0 + a \ln\left(\frac{V}{V_0}\right) + b_1 \ln\left(\frac{\theta_1}{\theta_{1,0}}\right) + b_2 \ln\left(\frac{\theta_2}{\theta_{2,0}}\right) \quad (3)$$

In Eq. (3), *a, b_1* and *b_2* are empirically determined constants, *V* is the fault slip rate, θ_1 and θ_2 are stable variables and the subscript '0' represents these quantities at an arbitrary reference state. Normally, most velocity step experiments can be well-described by a single state variable, although some velocity steps which are poorly fit by a 1-state variable RSF equation are better fit by a 2- state variable law (*Marone, 1998*) as described in Eq. (3). The RSF constants *a* and *b* are usually taken to represent some thermally-activated contact-scale Arrhenius-type process and a measure of the real area of asperity contact, respectively (*Ikari et al., 2016; Scholz, 2019*). The state variable, θ, represents contact age or contact lifetime (i.e., rapidly sliding contacts have a smaller contact age than slowly deforming contacts) and is represented as the ratio of a critical slip distance, D_c, and the asperity/contact sliding velocity. The evolution of frictional state (in a 1- or 2- state variable case) in response to a perturbation is usually expressed in one of two functional forms as the time-dependent Dieterich/aging law (*Dieterich, 1979*) or the slip-dependent Ruina/slip law (*Ruina, 1983*).

$$\frac{d\theta}{dt} = 1 - \frac{V\theta}{D_c} \qquad \text{(Aging Law)} \quad (4)$$

$$\frac{d\theta}{dt} = -\frac{V\theta}{D_c} \ln\left(\frac{V\theta}{D_c}\right) \quad \text{(Slip Law)} \quad (5)$$

We invert for the RSF parameters *a, b* and D_c using a least-squares procedure in RSFit3000 (*Skarbek and Savage, 2019*) by simultaneously solving Eqs. (3), and either (4) or (5) with a 1D elastic coupling equation described by

$$\frac{d\mu}{dt} = k(V_{lp} - V) \quad (6)$$

In Eq. (6), k represents the loading stiffness of the experiment and V_{lp} is the imposed shear rate. We only report values of the RSF parameters from those velocity steps where the coefficient of determination (R^2) is higher than 0.9. Thus, these inversions represent excellent fits to our experimental data. We performed RSF inversions using both the aging and slip laws for all velocity steps. However, we only report the RSF parameters from the aging law fits here since the slip law inversion consistently failed or had standard deviations greater than the mean value of the RSF parameter for higher sliding velocities. We quantify fault restrengthening by measuring frictional healing over different hold times during which the load point is held stationary (e.g., *Yasuhara et al., 2005*). We define frictional healing (*Dieterich, 1972; Beeler et al., 1994*) as the difference between peak friction upon re-shear after a hold and the previous steady state friction ($\Delta\mu_{Healing}$) (Figure 5a) and the healing rate, β, as the frictional healing per decade hold time (Figure 5b).

4. Results

4.1.Slide-Hold-Slide experiments

We observe distinctly different healing behaviors for the smectite-rich volcaniclastic facies and the chalks (Figure 5). The volcaniclastic conglomerates exhibit no post-hold peak friction upon reshear and near-zero healing rates (β = 0.0013/decade), similar to low values of frictional healing for clay-rich fault rocks and synthetic gouges reported in previous studies (e.g., *Saffer & Marone, 2003; Tesei et al. 2012;* Carpenter et al., 2012; *Carpenter et al., 2016)* for talc and montmorillonite gouges. On the other hand, the chalk lithology exhibits higher frictional healing, with healing rates (β = 0.0123/decade) (*Tesei et al., 2014*).

278 *4.2.Velocity stepping experiments*

279 Velocity stepping experiments allow us to define the rate-dependent friction parameter *(a-b)*
280 and invert individually for the RSF parameters *a*, *b* and D_c (Figure 6). Our results indicate that
281 *'a'* exhibits a modest velocity dependence (Figure 6a) while *'b'* is relatively insensitive to sliding
282 velocity (Figure 6b). Over a range of velocities spanning plate rates (0.0016 μm/s) to faster-than-
283 slow-slip rates (~300 μm/s), we document a bimodal behavior of friction velocity dependence
284 (Figure 6c). Specifically, the volcaniclastic conglomerates are largely velocity neutral or slightly
285 velocity weakening over slip rates ranging from plate-rate to slow slip rates at the northern
286 Hikurangi margin. At ~0.3 μm/s, this behavior transitions to a steady increase in the frictional
287 stability parameter *(a-b)* with fault slip rate for both the carbonates and the volcaniclastic facies.
288 This form of a second-order rate dependence of friction, i.e., the rate dependence of frictional
289 rate dependence has previously been documented in experiments conducted on a range of
290 material including synthetic mixtures of clay minerals and quartz (*Saffer et al., 2001; Ikari et al.,*
291 *2009; Kaproth and Marone, 2014*), and on natural samples from various tectonic settings (*Saito*
292 *et al., 2013; Rabinowitz et al., 2018*) including those that host shallow SSEs (*Saffer and Wallace,*
293 *2015*).

294 The critical slip distance, D_c, shows a slip rate dependence varying as $\sim\sqrt{V}$ over the range of
295 velocities explored (Figure 6d). Since we model some of our velocity steps with a single-state
296 variable formulation and others with the two-state variable equation, the D_c reported in Figure 6d
297 represents the (larger) D_{c2} for velocity steps where the 2- state variable RSF framework was used
298 to invert our experimental data. We do so because we are interested in determining the variation
299 of the total slip displacement required to reach a steady-state friction due to perturbations in the
300 driving velocity, and D_{c2} is a better representative of this quantity. Few studies have documented

a robust velocity dependence of D_c. However, our results closely match two cases where this velocity dependence has been documented in quartz gouge (*Mair and Marone, 1999*) and natural sediment (*Ikari et al., 2020b*) from the Waikukupa Thrust in southern New Zealand (Figure 6d). Our results demonstrating the velocity dependence of RSF parameters are consistent over a variety of hydration states (humid/saturated) and pore pressures (Figure 6c-d).

5. Discussion

Here we discuss the implications of the velocity dependence of the rate-state frictional parameters (*a, b* and D_c) in our experiments and those of others (*Mair and Marone, 1999; Ikari et al., 2020b*) for a range of different natural and synthetic fault gouges. A necessary criterion for the emergence of any kind of unstable slip in numerical simulations (*Gu et al., 1984; Im et al., 2020*) and laboratory experiments (e.g., *Leeman et al., 2016, 2018; Shreedharan et al., 2020*) is that the critical stiffness criterion be met. In other words, the fault loading stiffness (k) cannot exceed the critical rate of frictional weakening with slip (k_c) defined as

$$k \leq k_c = \frac{\sigma_{eff}(b-a)}{D_c} \quad (7)$$

In the framework described by Eq. (7), slow earthquakes naturally emerge when k approaches k_c (e.g., *Liu & Rice, 2007; Leeman et al., 2016*). This criterion can also be written in terms of a critical nucleation patch size, *h* (Dieterich, 1992)*, wherein the stiffness k is given by $k = \sim G/h^*$, where G represents a shear modulus. In this context, a larger slip patch at nucleation (h*) leads to a lower stiffness, and hence a greater tendency for instability to arise. From Eq. (7), one can observe that if the fault is velocity strengthening, i.e., *(a-b)* is positive, then the critical stiffness criterion can never be met since the positive fault stiffness can never be less than the negative critical stiffness. Thus, in this framework, a velocity strengthening fault cannot nucleate an

instability or rupture unless it is strongly perturbed (*Gu et al., 1984; McLaskey and Yamashita, 2017*).

5.1. Scaling of RSF parameters with slip rate

We observe that the RSF parameters *a, b* and D_c all increase with slip rate. This indicates that for a case where $k<k_c$ such that unstable slip may initiate, k_c decreases as slip velocity grows (i.e. during the nucleation phase of an instability), thus bringing it closer to *k* and energetically favoring slow rupture or stable sliding rather than an elastodynamic earthquake. This has been inferred from laboratory measurements (e.g., *Ikari et al.*, 2013; *Kaproth and Marone, 2013; Saffer & Wallace*, 2015; *Leeman et al., 2016, 2018*) and demonstrated by recent numerical simulations by *Im et al. (2020)* who assume a fault with velocity dependent *(a-b)* and D_c as we document here (Figure 6). Not only does this velocity-dependence favor slow slip, it increases the range of k/k_c values where slow slip is favored (*Im et al., 2020*). Numerical models have successfully incorporated the velocity-dependence of frictional stability *(a-b)* by using a cut-off velocity (e.g., *Shibazaki and Shimamoto, 2007; Rubin, 2008*) where the fault exhibits velocity-weakening friction below the cut-off velocity and transitions to a velocity-strengthening friction above this value. In our experiments, this transitional velocity apparently coincides with the peak slip rates of the shallow SSEs documented at the northern Hikurangi margin (Figure 6c), However, this does not preclude the possibility that instabilities hosted by these lithologies far exceed this threshold velocity (*Im et al., 2020*).

5.2. Mechanisms explaining the velocity dependence of the critical slip distance, D_c

346 Because D_c is a parameter that is difficult to directly estimate and may only be constrained
347 via inversion, we illustrate the velocity dependence of D_c directly by stacking multiple velocity
348 steps with different initial velocities (Figure 7a-b). Naturally, this gives rise to questions
349 surrounding the physical mechanisms that cause D_c to increase with slip rate. We explore dilatant
350 strengthening and broadening of the slip zone as a candidate mechanism for the velocity-
351 dependence of apparent or effective D_c (e.g., *Marone et al., 1990; Marone et al., 2009;*
352 *Samuelson et al., 2009, 2011*), in part, because it has been suggested as a mechanism that could
353 produce slow slip events (*Segall et al., 2010*). Dilatant strengthening is a mechanism where a
354 rapid increase in fault zone dilation as slip rate initially increases causes a transient undrained
355 decrease in local pore pressure, thus instantaneously increasing the local effective normal stress.
356 As fault slip velocity increases, the fault zone dilates producing a local drop in pore pressure.
357 This has been documented in lab studies as overprinting on the friction data by apparently
358 increasing the D_c or the distance over which the fault achieves a new steady-state friction
359 (*Samuelson et al., 2009, 2011*).
360 Based on our data showing velocity-dependent D_c in the 100% RH experiments (Figure 7b)
361 on the volcaniclastic facies and those by *Mair and Marone (1999)* on quartz gouge at room
362 humidity, we suggest that dilatant strengthening may not be the primary, intrinsic control on the
363 velocity-dependence of D_c. In the case of rough, planar (or saw-cut) faults, D_c is usually defined
364 as a microscopic asperity dimension (*Marone, 1998*). However, for our granular fault gouge with
365 a finite volume and numerous shear fabrics (e.g., *Kenigsberg et al., 2019*), we recast D_c as the
366 width of a localized shear zone. *Marone and Kilgore (1993)* have previously suggested this
367 interpretation of D_c for fault gouge based on their observations of decreasing D_c with increasing

shear strain, as the shear fabrics become more well-developed and deformation is increasingly accommodated in shear-parallel boundary and Y-shear fabrics.

We investigate dilatant strengthening as an additional possible mechanism by comparing velocity stepping experiments conducted in a saturated and pressurized fault to those on a fault in a 100% relative humidity environment (Figure 7a-b). We document higher values of D_c for higher sliding rates in both cases. However, while this increase is modest in the humid fault, i.e., ~10 – 75 μm for a 100x increase in loading velocity, the D_c increase is greater for the saturated fault (~40 – 250 μm for a 30x increase in loading velocity). As an additional validation exercise, we conduct velocity stepping experiments in four scenarios where the fault is pressurized to different degrees prior to shear at the same effective normal stress of 25 MPa (Figure 7c).

At higher P_P, the fault stabilizes and exhibits reduced slip weakening, lower values of the RSF parameter b and modestly higher values of D_c (Figure 7c and Supplementary Figure S1). The dependence of rate-state frictional parameters on P_P has previously been demonstrated in a limited number of studies (*Scuderi and Colletini, 2016; Xing et al., 2019; Bedford et al., 2021*). However, we note that due to the loading path (horizontal load is applied, then P_c, then P_p) in these experiments, there is also an unavoidable pre-compaction that scales with the amount of pore pressure applied. In this case, the different pre-compaction stresses would decrease the initial porosity and permeability of the fault and, by extension, dilatant strengthening to different degrees (*Samuelson et al., 2009*). Specifically, the experiment with largest pre-compaction stress (or lowest initial permeability) would experience the highest local pore pressure drop (and largest degree of dilatant strengthening) across a given velocity step. In other words, it is not possible to partition the stabilizing effects of P_P and the pre-compaction on the RSF parameters.

However, both stabilizing agents further support the possibility that dilatant strengthening is a non-trivial control on the velocity dependence of D_c.

Our results demonstrate the significant role of dilatant hardening on the 'apparent' values of RSF parameters via a competition between slip-dependent RSF parameters and time-dependent diffusion of fluids into the newly created pore spaces due to dilation. Moreover, our data are consistent with reports of dilatant strengthening on a range of gouge materials such as antigorite, olivine, quartz, chrysotile and serpentinite (*French and Zhu, 2017; Xing et al., 2019*) and direct observations of local pore-pressure drop during dynamic rupture in experimental faults (*Brantut, 2020*).

Thus, we suggest that velocity-dependent shear delocalization, and in turn, evolution of Dc, could be a significant factor in shallow SSE behavior, and future work could focus on validating/quantifying this hypothesis.

5.3.Mineralogical controls on frictional behavior

Significant lithological heterogeneities have been documented based on core sections recovered during IODP Expeditions 372/375 from Site U1520 (*Barnes et al., 2020*). Specifically, the dominant mineral types have been identified as carbonates and smectite-clays (Figure 2), occurring in the marls, chalk and volcaniclastic conglomerates. This represents an interplay of strength and frictional stability that could control the rich suite of shallow slip behaviors documented at the northern Hikurangi margin. The carbonate-rich chalk lithology is characterized by high frictional strength, high healing rates and frictional velocity-dependence spanning velocity-neutral to strengthening behaviors (Figure 8). Additionally, carbonate-bearing faults also undergo pressure solution enhanced healing at hydrothermal conditions (*Chen et al.,*

413 *2015, 2016*) which is not fully captured in our experiments due to relatively short (maximum
414 3000s) hold times and room temperature conditions. Thus, we anticipate that our healing rates
415 represent a lower bound on the potential healing that carbonates could undergo. In contrast, the
416 deeper (>850 mbsf) smectite-rich volcaniclastic conglomerates are frictionally weak, and are
417 velocity strengthening at slip rates over 0.1 μm/s (Figure 8). This response indicates that the
418 frictional behavior of the clay-fractions dominates the frictional response of volcaniclastic
419 conglomerates. Our observations are consistent with numerous studies documenting that as little
420 as 20% (by weight) of phyllosilicate-fraction can dominate the frictional behavior of mixed
421 gouge (*Logan and Rauenzahn, 1987; Saffer and Marone, 2003; Ikari et al., 2007; Giorgetti et*
422 *al., 2015*). Finally, marls composed of ~35% phyllosilicates, 50% carbonates and 15% quartz +
423 feldspars are characterized by an intermediate frictional response between the chalk and
424 volcaniclastic lithologies.

425 We integrate our experimental measurements of healing with geodetically derived constraints
426 from stress drop and recurrence interval of SSEs at the Hikurangi margin and seismologically
427 estimated stress drops for a global catalog of fast earthquakes (Figure 9). Specifically, we
428 constrain healing for 'ordinary' earthquakes using a global catalog of fast, elastodynamic
429 seismicity with relatively well-resolved recurrence intervals (*Kanamori and Allen, 1986*), and
430 estimate their stress drops from moment magnitudes using a circular crack model (*Brune, 1970*).
431 These earthquakes represent a moment magnitude, M_w, range of 5.6-7.8 and recurrence times of
432 the order of ~50 – 60000 years (*Kanamori and Allen, 1986*). Based on fits to the log-linear
433 relationship between the static stress drop and recurrence times for these earthquakes, we
434 estimate an average healing rate of ~1.6 MPa/decade. Because these earthquakes represent a
435 range of depths and hydrothermal conditions which could control healing rates (*Carpenter et al.,*

436 *2016*), our calculations provide a qualitative estimate of healing rates which can be compared
437 with SSEs. However, the relatively high healing rates that we document here are consistent with
438 earthquake nucleation in predominantly quartzofeldspathic crystalline basement (*Carpenter et*
439 *al., 2012; Carpenter et al., 2016*). Our observations of the stress drop – recurrence time
440 relationship for SSEs at the northern Hikurangi margin (*Wallace and Beavan, 2010; Bartlow et*
441 *al., 2014*) low healing and small stress drops (~ 10s of kPa) for the shallow SSEs in this region.
442 This is consistent with the low static stress-drop model of SSE nucleation (*Brodsky and Mori,*
443 *2007; Ide et al., 2007; Segall et al., 2010*) and low inferred values of stress drops associated with
444 the northern Hikurangi SSEs (*Bartlow et al., 2014*) and SSEs globally (*Bürgmann, 2018*).
445 Our experimental estimates of healing (and healing rates) in the chalk and volcaniclastic
446 facies provide depth-dependent constraints on healing rates when extrapolated to hold times
447 consistent with the recurrence duration of the quasi-periodic shallow SSEs at the northern
448 Hikurangi margin. Specifically, we consider two end-member scenarios to estimate maximum
449 and minimum stress healing rates (MPa/decade) for mixtures of the subducting sediments – a
450 carbonate-rich fault and little/no pore-fluid overpressures representing the highest healing rates,
451 and a smectite-rich fault with significant (locally undrained) overpressures representing the
452 lowest healing rates at an effective stress of 25 MPa. The geodetically defined healing rate (0.1
453 MPa/decade) is intermediate between the high healing rates (~0.31 MPa/decade) of carbonate
454 faults and the lower healing rates (~0.03 MPa/decade) of the volcaniclastic conglomerates.
455 Broadly, our results indicate that mixing between the strong, brittle carbonates and the weak,
456 viscous clay minerals could be an important two-phase mineralogical control on healing and
457 shallow SSE nucleation at the northern Hikurangi margin, consistent with structural observations
458 by *Leah et al. (2020)*. Because the shallow portion of the northern Hikurangi margin is relatively

459 cold (*McCaffrey et al., 2008*), we do not consider the role of temperature here, but it could be an
460 additional control at depth, particularly downdip of the seismogenic zone.
461
462 *5.4.Implications for shallow SSEs at the northern Hikurangi Margin*
463 We present a conceptual model of subduction at the Hikurangi margin based on our
464 observations of velocity-dependent friction and the strong mineralogical controls on frictional
465 behavior (Figure 10). In this model, frictional (carbonates, seamounts) and geometric
466 (seamounts) asperities on the downgoing plate are embedded in (or mix with) a viscous matrix of
467 predominantly velocity-neutral, frictionally weak volcaniclastic conglomerates which exhibit
468 low healing rates, indicating an inability to store elastic strain energy over long timescales.
469 Shallow instabilities may nucleate in the strong, velocity-strengthening carbonates with high
470 healing rates at modestly elevated temperatures and/or stresses (~70^0C; *Ikari et al., 2013;*
471 *Kurzawski et al., 2016*). However, a combination of intrinsically velocity-dependent friction (i.e.,
472 velocity-dependence of a-b and D_c) and dilatant strengthening enhanced by potentially over-
473 pressurized pore-fluids may arrest these instabilities, thus manifesting as shallow slow
474 earthquakes. Shallow instabilities nucleating in the basaltic seamounts, depending on the degree
475 of alteration experienced by the basalts (*Cox, 1990; Ikari et al., 2020c*), could also propagate as
476 SSEs. Further, numerical models of shallow SSEs incorporating a cut-off velocity (*Shibazaki et*
477 *al., 2019)* or explicit velocity dependence of friction parameters (*Im et al., 2020*) have
478 qualitatively reproduced the range of slip behaviors documented here. At seismogenic depths
479 (>7-10 km), pressure-temperature conditions are conducive for carbonates to be significantly
480 velocity weakening at all slip rates (eg. *Ikari et al., 2013; Kurzawski et al., 2016*), and thus,
481 carbonates and/or basalts may nucleate instabilities that grow to be fast, dynamic earthquakes. In

such cases, dynamic weakening could dominate in the shallower velocity-neutral/strengthening sediments thus preventing the ruptures from arresting (*Di Toro et al., 2011; Faulkner et al., 2011; Aretusini et al., 2021*). Our conceptual model, motivated by experimental results indicating the strong role of the clay-rich volcaniclastic conglomerates and the second-order velocity-dependence of friction in modulating shallow slip behavior, provides insights into the mechanics of shallow SSEs at the northern Hikurangi margin.

6. Conclusions

We present a suite of friction experiments conducted on input material to the Hikurangi subduction margin recovered during IODP Expeditions 372/375. Specifically, we quantify the frictional strength, stability and healing behavior of the two dominant lithologies – carbonates and smectite-rich volcaniclastic conglomerates. We present velocity-dependent frictional parameters *(a-b)* and D_c as potentially important controls on shallow slow earthquake nucleation here. In particular, the transition in *(a-b)* from velocity-weakening to strengthening behavior with increasing velocity could act as a rate-limiting agent, and the velocity-dependent increase in D_c increases frictional stability by reducing the critical fault stiffness (or increasing the critical nucleation dimension) further favoring slower slip. Based on velocity-stepping experiments conducted on saturated and room-dry (humid) faults, we conclude that the velocity-dependence of D_c is likely due to a combination of dilatant strengthening and shear zone delocalization at higher fault slip rates. Finally, we compare experimentally determined frictional healing rates with geodetically-inferred recurrence rates to demonstrate that the shallow slow earthquakes at the northern Hikurangi margin could be hosted by a mixture of strong, brittle carbonates and weak, viscous clay-rich sediments. Our results provide additional insights and constraints into

505 the mechanics of shallow slow slip at the northern Hikurangi margin, and set the path for future
506 investigations into the role of frictional heterogeneities on shallow SSEs.

507 **Table 1.** List of experiments and boundary conditions

Experiment No.	Sample Name	Apparatus	Effective normal stress, σ_{eff} (MPa)	Pore pressure, P_p	Saturation state	Shear velocities (μm/s)
p5200	U1520C13R4	Biaxial	25	0	100% RH	1-1000
p5391	U1520C38R5	Biaxial	25	5	Saturated	0.3-300
p5392	U1520C28R5	Biaxial	25	5	Saturated	0.3-300
p5393	U1520C19R2	Biaxial	25	5	Saturated	0.3-300
p5419	U1520C28R5	Biaxial	25	0, 17	Saturated	0.3-1000
p5454	U1520C28R5	Biaxial	25	0	100% RH	0.3-1000
B875gds	U1520C38R2	Plate-rate	25	0	Saturated	0.00165-1.65
B984gds	U1520C19R1	Plate-rate	25	0	Saturated	0.0016-1.65

508

509 **Figures**

510 **Figure 1.** (a) Map of New Zealand showing the Hikurangi Trough and interface between the
511 subducting Pacific and overlying Australian plates. The black line and red dots show the location
512 of seismic line 05CM-04 and IODP Expedition 372/375 drill-sites respectively. Black curves on
513 the upper plate show 50 mm slip contours from the 2014 SSE (*Wallace et al., 2016*). (b) Two-
514 way travel time (TWTT) versus Common Depth Point (CDP) for processed seismic line 05CM-
515 04 showing the locations of various drill sites targeted during IODP Expedition 375, the
516 hypocenter of the 1947 Tsunami earthquake (red star) and a proposed subducting seamount at the
517 subduction plate interface (*After Gray et al., 2019*)

518

519 **Figure 2.** Depth section of various lithostratigraphic units at site U1520 and bulk sediment
520 mineralogical composition of the samples used in this study.

521

522 **Figure 3.** Schematic of experimental apparatuses used in this study. (a) Samples in the biaxial
523 apparatus are sheared in a double direct-shear configuration in a true-triaxial stress state with
524 independent inlet (PpA) and outlet (PpB) pore fluid reservoirs. Normal and shear stresses are
525 supplied by a horizontal and vertical piston respectively. The sample rests in a pressure vessel
526 and is separated from the surrounding confining fluid (oil) by a rubber jacket. Inset to (a) shows
527 the powdered sample (gouge) sandwiched between three grooved steel blocks with internal
528 plumbing for pore fluid flow. (b) Samples in the plate rate apparatus are saturated and sheared in
529 a single direct-shear configuration with a fixed top plate and a moving base plate. A vertical
530 piston supplies the normal load and a horizontal piston supplies the shear load.

531

532 **Figure 4.** A plot of friction versus loadpoint displacement for a representative experimental run
533 shows various aspects of each experiment including unload/reload cycles to constrain initial
534 loading stiffness, velocity step sequences and slide-hold-slide sequences. Inset to the plot shows
535 the evolution of friction for a velocity step from 30 to 100 μm/s.
536
537 **Figure 5.** Friction evolution during slide-hold-slide experiments (a) and healing rates (b) in
538 volcaniclastic conglomerates (black) and carbonates (blue) shows the significantly higher
539 frictional healing rates in carbonates as compared to the clay-rich volcaniclastics.
540
541 **Figure 6.** Evolution of rate-state friction (RSF) parameters with fault initial velocity prior to an
542 upstep for (a) RSF parameter '*a*' (b) RSF parameter '*b*' (c) the difference (*a*-*b*) which marks the
543 fault frictional stability as velocity weakening (VW) or velocity strengthening (VS) and (d) the
544 critical slip distance, D_c. Different colors represent different material/samples and the symbols
545 represent biaxial (square) and plate-rate (circle) apparatuses.
546
547 **Figure 7.** Evolution of the critical slip distance, D_c, with fault slip rate and pore pressure in
548 experiments conducted on the clay-rich volcaniclastic conglomerates from sample U1520 28R5.
549 (a) Overlay of four velocity steps in experiment with P_P = 17 MPa shows that it takes more
550 displacement for the friction to reach a post-step steady-state value for velocity steps at higher
551 velocities. (b) Overlay of four velocity steps in experiment with 100% relative humidity (RH)
552 shows that it takes more displacement for the friction to reach a post-step steady-state value for
553 velocity steps at higher velocities, even with no pore fluids. (c) matrix of different velocity steps
554 at different hydration states shows the velocity dependence of D_c and the 'evolution' effect for

555 all values of P_P. However, this effect is more prominent for larger P_P values likely due to
556 dilatational hardening.
557
558 **Figure 8.** Variation of (a) coefficient of friction (b) healing rate and (c) frictional stability, *(a-b)*
559 with depth at site U1520. Different colors represent different material/samples and the symbols
560 represent biaxial (square) and plate-rate (circle) apparatuses.
561
562 **Figure 9.** Compilation of fault healing from slide-hold-slide experiments in this study and
563 earthquake stress drops for the northern Hikurangi slow earthquakes (*Wallace and Beavan,*
564 *2010; Bartlow et al., 2014*) and a global catalog of fast earthquakes (*Kanamori and Allen, 1986*)
565 shows the remarkably low healing rates for the clay-rich volcaniclastic samples tested in this
566 study and the shallow slow earthquakes at the northern Hikurangi margin.
567
568 **Figure 10.** Illustrative cartoon showing summary of potential frictional and lithological controls
569 on slow and fast earthquakes at the northern Hikurangi margin. In this view carbonate-rich
570 patches and seamounts make up asperity patches in a velocity neutral/strengthening matrix of the
571 abundant clay-rich volcaniclastic material at the plate interface. The volcaniclastic inputs to the
572 plate interface at the northern Hikurangi margin are characterized by velocity-neutral friction at
573 low slip rates transitioning to velocity strengthening friction at ~3 μm/s, velocity-dependent D_c
574 and exhibit extremely low (or zero) healing rates. The carbonate patches are nominally velocity
575 strengthening at high slip rates, have velocity dependent D_c and exhibit high healing rates at
576 shallow depths consistent with the slow earthquakes. In this model, a carbonate asperity could
577 nucleate a shallow instability whose slip rate is modulated by a combination of the inherent

578 velocity dependence of friction (a-b and D_c) and dilatational hardening at high pore pressures
579 which further enhances the velocity dependence of D_c.

580

581 **Acknowledgements**

582 We thank Steven Swavely for technical assistance with the biaxial experiments. This study was
583 supported by a US Science Support Program Schlanger Ocean Drilling Fellowship and a Post-
584 Expedition Award to S.S., European Research Council Advance Grant 835012 (TECTONIC),
585 the US Department of Energy grants DESC0020512 and DE-EE0008763, and the US National
586 Science Foundation grants EAR 1520760, EAR 1547441, and EAR 1763305 to C. Marone.
587 Experimental data used in this study can be retrieved from
588 https://doi.org/10.5281/zenodo.5199953.

589

590 **References**

591 Ando, R., Nakata, R., & Hori, T. (2010). A slip pulse model with fault heterogeneity for low-
592 frequency earthquakes and tremor along plate interfaces. Geophysical Research Letters,
593 37(10).
594 Araki, E., Saffer, D. M., Kopf, A. J., Wallace, L. M., Kimura, T., Machida, Y., ... & Expedition,
595 I. O. D. P. (2017). Recurring and triggered slow-slip events near the trench at the Nankai
596 Trough subduction megathrust. Science, 356(6343), 1157-1160.
597 Aretusini, S., Meneghini, F., Spagnuolo, E., Harbord, C. W., & Di Toro, G. (2021). Fluid
598 pressurisation and earthquake propagation in the Hikurangi subduction zone. Nature
599 Communications, 12(1), 1-8.
600 Barker, D. H., Henrys, S., Caratori Tontini, F., Barnes, P. M., Bassett, D., Todd, E., & Wallace,
601 L. (2018). Geophysical constraints on the relationship between seamount subduction, slow
602 slip, and tremor at the north Hikurangi subduction zone, New Zealand. Geophysical Research
603 Letters, 45(23), 12-804.
604 Barnes et al., 2019. Site U1520. In Wallace, L.M., Saffer, D.M., Barnes, P.M., Pecher, I.A.,
605 Petronotis, K.E., LeVay, L.J., and the Expedition 372/375 Scientists, Hikurangi Subduction
606 Margin Coring, Logging, and Observatories. Proceedings of the International Ocean
607 Discovery Program, 372B/375: College Station, TX (International Ocean Discovery
608 Program). https://doi.org/10.14379/iodp.proc.372B375.105.2019

609 Barnes, P. M., Wallace, L. M., Saffer, D. M., Bell, R. E., Underwood, M. B., Fagereng, A., ... &
610 Kitajima, H. (2020). Slow slip source characterized by lithological and geometric
611 heterogeneity. Science Advances, 6(13), eaay3314.
612 Bartlow, N. M., Wallace, L. M., Beavan, R. J., Bannister, S., & Segall, P. (2014). Time-
613 dependent modeling of slow slip events and associated seismicity and tremor at the
614 Hikurangi subduction zone, New Zealand. Journal of Geophysical Research: Solid Earth,
615 119(1), 734-753.
616 Bassett, D., Sutherland, R., & Henrys, S. (2014). Slow wavespeeds and fluid overpressure in a
617 region of shallow geodetic locking and slow slip, Hikurangi subduction margin, New
618 Zealand. Earth and Planetary Science Letters, 389, 1-13.
619 Bedford, J., Faulkner, D., Allen, M., & Hirose, T. (2021). The stabilizing effect of high pore-
620 fluid pressure along subduction megathrust faults: Evidence from friction experiments on
621 accretionary sediments from the Nankai Trough. EarthArXiv.
622 https://doi.org/10.31223/X5SP6Q
623 Beeler, N. M., Tullis, T. E., & Weeks, J. D. (1994). The roles of time and displacement in the
624 evolution effect in rock friction. *Geophysical Research Letters*, *21*(18), 1987-1990.
625 Bell, R., Sutherland, R., Barker, D. H., Henrys, S., Bannister, S., Wallace, L., & Beavan, J.
626 (2010). Seismic reflection character of the Hikurangi subduction interface, New Zealand, in
627 the region of repeated Gisborne slow slip events. Geophysical Journal International, 180(1),
628 34-48.
629 Bell, R., Holden, C., Power, W., Wang, X., & Downes, G. (2014). Hikurangi margin tsunami
630 earthquake generated by slow seismic rupture over a subducted seamount. Earth and
631 Planetary Science Letters, 397, 1-9.
632 Boulton, C., Niemeijer, A. R., Hollis, C. J., Townend, J., Raven, M. D., Kulhanek, D. K., &
633 Shepherd, C. L. (2019). Temperature-dependent frictional properties of heterogeneous
634 Hikurangi Subduction Zone input sediments, ODP Site 1124. Tectonophysics, 757, 123-139.
635 Brantut, N. (2020). Dilatancy-induced fluid pressure drop during dynamic rupture: Direct
636 experimental evidence and consequences for earthquake dynamics. *Earth and Planetary*
637 *Science Letters*, *538*, 116179.
638 Brodsky, E. E., & Mori, J. (2007). Creep events slip less than ordinary earthquakes. *Geophysical*
639 *Research Letters*, *34*(16).
640 Brune, J. N. (1970). Tectonic stress and the spectra of seismic shear waves from earthquakes.
641 Journal of geophysical research, 75(26), 4997-5009.
642 Bürgmann, R. (2018). The geophysics, geology and mechanics of slow fault slip. Earth and
643 Planetary Science Letters, 495, 112-134.
644 Carpenter, B. M., Marone, C., & Saffer, D. M. (2011). Weakness of the San Andreas Fault
645 revealed by samples from the active fault zone. *Nature Geoscience*, *4*(4), 251-254.
646 Carpenter, B. M., Saffer, D. M., & Marone, C. (2012). Frictional properties and sliding stability
647 of the San Andreas fault from deep drill core. Geology, 40(8), 759-762.
648 Carpenter, B. M., Ikari, M. J., & Marone, C. (2016). Laboratory observations of time-dependent
649 frictional strengthening and stress relaxation in natural and synthetic fault gouges. Journal of
650 Geophysical Research: Solid Earth, 121(2), 1183-1201.
651 Chen, J., Verberne, B. A., & Spiers, C. J. (2015). Interseismic re-strengthening and stabilization
652 of carbonate faults by “non-Dieterich” healing under hydrothermal conditions. Earth and
653 Planetary Science Letters, 423, 1-12.

Chen, J., & Spiers, C. J. (2016). Rate and state frictional and healing behavior of carbonate fault gouge explained using microphysical model. Journal of Geophysical Research: Solid Earth, 121(12), 8642-8665.

Cox, S. J. D. (1990). Velocity-dependent friction in a large direct shear experiment on gabbro. Geological Society, London, Special Publications, 54(1), 63-70.

Dieterich, J. H. (1972). Time-dependent friction in rocks. *Journal of Geophysical Research*, *77*(20), 3690-3697.

Dieterich, J. H. (1978). Time-dependent friction and the mechanics of stick-slip. In Rock friction and earthquake prediction (pp. 790-806). Birkhäuser, Basel.

Dieterich, J. H. (1979). Modeling of rock friction: 1. Experimental results and constitutive equations. Journal of Geophysical Research: Solid Earth, 84(B5), 2161-2168.

Dieterich, J. H. (1992). Earthquake nucleation on faults with rate-and state-dependent strength. Tectonophysics, 211(1-4), 115-134.

Di Toro, G., Han, R., Hirose, T., De Paola, N., Nielsen, S., Mizoguchi, K., ... & Shimamoto, T. (2011). Fault lubrication during earthquakes. Nature, 471(7339), 494-498.

Ellis, S., Fagereng, Å., Barker, D., Henrys, S., Saffer, D., Wallace, L., ... & Harris, R. (2015). Fluid budgets along the northern Hikurangi subduction margin, New Zealand: The effect of a subducting seamount on fluid pressure. *Geophysical Journal International*, *202*(1), 277-297.

Faulkner, D. R., Mitchell, T. M., Behnsen, J., Hirose, T., & Shimamoto, T. (2011). Stuck in the mud? Earthquake nucleation and propagation through accretionary forearcs. Geophysical Research Letters, 38(18).

French, M. E., & Zhu, W. (2017). Slow fault propagation in serpentinite under conditions of high pore fluid pressure. Earth and Planetary Science Letters, 473, 131-140.

Frye, K. M., & Marone, C. (2002). Effect of humidity on granular friction at room temperature. Journal of Geophysical Research: Solid Earth, 107(B11), ETG-11.

Giorgetti, C., Carpenter, B. M., & Collettini, C. (2015). Frictional behavior of talc-calcite mixtures. Journal of Geophysical Research: Solid Earth, 120(9), 6614-6633.

Gray, M., Bell, R. E., Morgan, J. V., Henrys, S., Barker, D. H., & IODP Expedition 372 and 375 science parties. (2019). Imaging the shallow subsurface structure of the North Hikurangi Subduction Zone, New Zealand, using 2-D full-waveform inversion. Journal of Geophysical Research: Solid Earth, 124(8), 9049-9074.

Gu, J. C., Rice, J. R., Ruina, A. L., & Simon, T. T. (1984). Slip motion and stability of a single degree of freedom elastic system with rate and state dependent friction. Journal of the Mechanics and Physics of Solids, 32(3), 167-196.

Ide, S., Beroza, G. C., Shelly, D. R., & Uchide, T. (2007). A scaling law for slow earthquakes. Nature, 447(7140), 76-79.

Ikari, M. J., Saffer, D. M., & Marone, C. (2007). Effect of hydration state on the frictional properties of montmorillonite-based fault gouge. Journal of Geophysical Research: Solid Earth, 112(B6).

Ikari, M. J., Saffer, D. M., & Marone, C. (2009). Frictional and hydrologic properties of clay-rich fault gouge. *Journal of Geophysical Research: Solid Earth*, *114*(B5).

Ikari, M. J., & Saffer, D. M. (2011). Comparison of frictional strength and velocity dependence between fault zones in the Nankai accretionary complex. *Geochemistry, Geophysics, Geosystems*, *12*(4).

Ikari, M. J., Marone, C., Saffer, D. M., & Kopf, A. J. (2013). Slip weakening as a mechanism for slow earthquakes. Nature geoscience, 6(6), 468-472.

Ikari, M. J., Ito, Y., Ujiie, K., & Kopf, A. J. (2015). Spectrum of slip behaviour in Tohoku fault zone samples at plate tectonic slip rates. Nature Geoscience, 8(11), 870-874.

Ikari, M. J., Carpenter, B. M., & Marone, C. (2016). A microphysical interpretation of rate-and state-dependent friction for fault gouge. Geochemistry, Geophysics, Geosystems, 17(5), 1660-1677.

Ikari, M. J., Wallace, L. M., Rabinowitz, H. S., Savage, H. M., Hamling, I. J., & Kopf, A. J. (2020a). Observations of Laboratory and Natural Slow Slip Events: Hikurangi Subduction Zone, New Zealand. Geochemistry, Geophysics, Geosystems, 21(2), e2019GC008717.

Ikari, M. J., Carpenter, B. M., Scuderi, M. M., Collettini, C., & Kopf, A. J. (2020b). Frictional Strengthening Explored During Non-Steady State Shearing: Implications for Fault Stability and Slip Event Recurrence Time. Journal of Geophysical Research: Solid Earth, 125(10), e2020JB020015.

Ikari, M. J., Wilckens, F. K., & Saffer, D. M. (2020c). Implications of basement rock alteration in the Nankai Trough, Japan for subduction megathrust slip behavior. Tectonophysics, 774, 228275.

Im, K., Saffer, D., Marone, C., & Avouac, J. P. (2020). Slip-rate-dependent friction as a universal mechanism for slow slip events. Nature Geoscience, 13(10), 705-710.

Kanamori, H., & Allen, C. R. (1986). Earthquake repeat time and average stress drop.

Kaproth, B. M., & Marone, C. (2013). Slow earthquakes, preseismic velocity changes, and the origin of slow frictional stick-slip. Science, 341(6151), 1229-1232.

Kaproth, B. M., & Marone, C. (2014). Evolution of elastic wave speed during shear-induced damage and healing within laboratory fault zones. Journal of Geophysical Research: Solid Earth, 119(6), 4821-4840.

Kato, A., Obara, K., Igarashi, T., Tsuruoka, H., Nakagawa, S., & Hirata, N. (2012). Propagation of slow slip leading up to the 2011 Mw 9.0 Tohoku-Oki earthquake. Science, 335(6069), 705-708.

Kenigsberg, A. R., Rivière, J., Marone, C., & Saffer, D. M. (2019). The effects of shear strain, fabric, and porosity evolution on elastic and mechanical properties of clay-rich fault gouge. Journal of Geophysical Research: Solid Earth, 124(11), 10968-10982.

Kurzawski, R. M., Stipp, M., Niemeijer, A. R., Spiers, C. J., & Behrmann, J. H. (2016). Earthquake nucleation in weak subducted carbonates. Nature Geoscience, 9(9), 717-722.

Leah, H., Fagereng, Å., Meneghini, F., Morgan, J. K., Savage, H. M., Wang, M., ... & Ikari, M. J. (2020). Mixed brittle and viscous strain localization in pelagic sediments seaward of the Hikurangi Margin, New Zealand. Tectonics, 39(8), e2019TC005965.

Leeman, J. R., Saffer, D. M., Scuderi, M. M., & Marone, C. (2016). Laboratory observations of slow earthquakes and the spectrum of tectonic fault slip modes. Nature communications, 7(1), 1-6.

Leeman, J. R., Marone, C., & Saffer, D. M. (2018). Frictional mechanics of slow earthquakes. Journal of Geophysical Research: Solid Earth, 123(9), 7931-7949.

Liu, Y., & Rice, J. R. (2007). Spontaneous and triggered aseismic deformation transients in a subduction fault model. Journal of Geophysical Research: Solid Earth, 112(B9).

Logan, J. M., & Rauenzahn, K. A. (1987). Frictional dependence of gouge mixtures of quartz and montmorillonite on velocity, composition and fabric. *Tectonophysics*, *144*(1-3), 87-108.

Mair, K., & Marone, C. (1999). Friction of simulated fault gouge for a wide range of velocities and normal stresses. Journal of Geophysical Research: Solid Earth, 104(B12), 28899-28914.

745 Marone, C., Raleigh, C. B., & Scholz, C. H. (1990). Frictional behavior and constitutive
746 modeling of simulated fault gouge. Journal of Geophysical Research: Solid Earth, 95(B5),
747 7007-7025.
748 Marone, C., & Kilgore, B. (1993). Scaling of the critical slip distance for seismic faulting with
749 shear strain in fault zones. Nature, 362(6421), 618-621.
750 Marone, C. (1998). Laboratory-derived friction laws and their application to seismic faulting.
751 Annual Review of Earth and Planetary Sciences, 26(1), 643-696.
752 Marone, C., Cocco, M., Richardson, E., & Tinti, E. (2009). The critical slip distance for seismic
753 and aseismic fault zones of finite width. *International Geophysics*, *94*, 135-162.
754 McCaffrey, R., Wallace, L. M., & Beavan, J. (2008). Slow slip and frictional transition at low
755 temperature at the Hikurangi subduction zone. Nature Geoscience, 1(5), 316-320.
756 McLaskey, G. C., & Yamashita, F. (2017). Slow and fast ruptures on a laboratory fault
757 controlled by loading characteristics. Journal of Geophysical Research: Solid Earth, 122(5),
758 3719-3738.
759 Meng, L., Huang, H., Bürgmann, R., Ampuero, J. P., & Strader, A. (2015). Dual megathrust slip
760 behaviors of the 2014 Iquique earthquake sequence. Earth and Planetary Science Letters,
761 411, 177-187.
762 Nakata, R., Ando, R., Hori, T., & Ide, S. (2011). Generation mechanism of slow earthquakes:
763 Numerical analysis based on a dynamic model with brittle-ductile mixed fault heterogeneity.
764 Journal of Geophysical Research: Solid Earth, 116(B8).
765 Peng, Z., & Gomberg, J. (2010). An integrated perspective of the continuum between
766 earthquakes and slow-slip phenomena. Nature geoscience, 3(9), 599-607.
767 Rabinowitz, H. S., Savage, H. M., Skarbek, R. M., Ikari, M. J., Carpenter, B. M., & Collettini, C.
768 (2018). Frictional behavior of input sediments to the Hikurangi Trench, New Zealand.
769 Geochemistry, Geophysics, Geosystems, 19(9), 2973-2990.
770 Rubin, A. M. (2008). Episodic slow slip events and rate-and-state friction. Journal of
771 Geophysical Research: Solid Earth, 113(B11).
772 Ruina, A. (1983). Slip instability and state variable friction laws. Journal of Geophysical
773 Research: Solid Earth, 88(B12), 10359-10370.
774 Saffer, D. M., Frye, K. M., Marone, C., & Mair, K. (2001). Laboratory results indicating
775 complex and potentially unstable frictional behavior of smectite clay. Geophysical Research
776 Letters, 28(12), 2297-2300.
777 Saffer, D. M., & Marone, C. (2003). Comparison of smectite-and illite-rich gouge frictional
778 properties: application to the updip limit of the seismogenic zone along subduction
779 megathrusts. Earth and Planetary Science Letters, 215(1-2), 219-235.
780 Saffer, D. M., & Wallace, L. M. (2015). The frictional, hydrologic, metamorphic and thermal
781 habitat of shallow slow earthquakes. Nature Geoscience, 8(8), 594-600.
782 Saito, T., Ujiie, K., Tsutsumi, A., Kameda, J., & Shibazaki, B. (2013). Geological and frictional
783 aspects of very-low-frequency earthquakes in an accretionary prism. Geophysical research
784 letters, 40(4), 703-708.
785 Samuelson, J., Elsworth, D., & Marone, C. (2009). Shear-induced dilatancy of fluid-saturated
786 faults: Experiment and theory. Journal of Geophysical Research: Solid Earth, 114(B12).
787 Samuelson, J., Elsworth, D., & Marone, C. (2011). Influence of dilatancy on the frictional
788 constitutive behavior of a saturated fault zone under a variety of drainage conditions. Journal
789 of Geophysical Research: Solid Earth, 116(B10).
790 Scholz, C. H. (2019). The mechanics of earthquakes and faulting. Cambridge university press.

Schwartz, S. Y., & Rokosky, J. M. (2007). Slow slip events and seismic tremor at circum-Pacific subduction zones. Reviews of Geophysics, 45(3).

Scuderi, M. M., & Collettini, C. (2016). The role of fluid pressure in induced vs. triggered seismicity: Insights from rock deformation experiments on carbonates. *Scientific reports*, *6*(1), 1-9.

Scuderi, M. M., Collettini, C., Viti, C., Tinti, E., & Marone, C. (2017). Evolution of shear fabric in granular fault gouge from stable sliding to stick slip and implications for fault slip mode. Geology, 45(8), 731-734.

Segall, P., Rubin, A. M., Bradley, A. M., & Rice, J. R. (2010). Dilatant strengthening as a mechanism for slow slip events. Journal of Geophysical Research: Solid Earth, 115(B12).

Shibazaki, B., & Shimamoto, T. (2007). Modelling of short-interval silent slip events in deeper subduction interfaces considering the frictional properties at the unstable—stable transition regime. Geophysical Journal International, 171(1), 191-205.

Shibazaki, B., Wallace, L. M., Kaneko, Y., Hamling, I., Ito, Y., & Matsuzawa, T. (2019). Three-Dimensional Modeling of Spontaneous and Triggered Slow-Slip Events at the Hikurangi Subduction Zone, New Zealand. *Journal of Geophysical Research: Solid Earth*, *124*(12), 13250-13268.

Shreedharan, S., Bolton, D. C., Rivière, J., & Marone, C. (2020). Preseismic fault creep and elastic wave amplitude precursors scale with lab earthquake magnitude for the continuum of tectonic failure modes. Geophysical Research Letters, 47(8), e2020GL086986.

Skarbek, R. M., Rempel, A. W., & Schmidt, D. A. (2012). Geologic heterogeneity can produce aseismic slip transients. Geophysical Research Letters, 39(21).

Skarbek, R. M., & Savage, H. M. (2019). RSFit3000: A MATLAB GUI-based program for determining rate and state frictional parameters from experimental data. Geosphere, 15(5), 1665-1676.

Tesei, T., Collettini, C., Carpenter, B. M., Viti, C., & Marone, C. (2012). Frictional strength and healing behavior of phyllosilicate-rich faults. Journal of Geophysical Research: Solid Earth, 117(B9).

Tesei, T., Collettini, C., Barchi, M. R., Carpenter, B. M., & Di Stefano, G. (2014). Heterogeneous strength and fault zone complexity of carbonate-bearing thrusts with possible implications for seismicity. Earth and Planetary Science Letters, 408, 307-318.

Todd, E. K., Schwartz, S. Y., Mochizuki, K., Wallace, L. M., Sheehan, A. F., Webb, S. C., ... & Henrys, S. (2018). Earthquakes and tremor linked to seamount subduction during shallow slow slip at the Hikurangi margin, New Zealand. Journal of Geophysical Research: Solid Earth, 123(8), 6769-6783.

Ujiie, K., Tanaka, H., Saito, T., Tsutsumi, A., Mori, J. J., Kameda, J., ... & Toczko, S. (2013). Low coseismic shear stress on the Tohoku-Oki megathrust determined from laboratory experiments. *Science*, *342*(6163), 1211-1214.

Underwood, M. B. (2020). Data report: reconnaissance of bulk sediment composition and clay mineral assemblages: inputs to the Hikurangi subduction system. Proceedings of the International Ocean Discovery Program, 372.

Wallace, L. M., Beavan, J., McCaffrey, R., & Darby, D. (2004). Subduction zone coupling and tectonic block rotations in the North Island, New Zealand. Journal of Geophysical Research: Solid Earth, 109(B12).

Wallace, L. M., & Beavan, J. (2010). Diverse slow slip behavior at the Hikurangi subduction margin, New Zealand. Journal of Geophysical Research: Solid Earth, 115(B12).

837 Wallace, L. M., Bartlow, N., Hamling, I., & Fry, B. (2014). Quake clamps down on slow slip.
838 Geophysical Research Letters, 41(24), 8840-8846.
839 Wallace, L. M., Webb, S. C., Ito, Y., Mochizuki, K., Hino, R., Henrys, S., ... & Sheehan, A. F.
840 (2016). Slow slip near the trench at the Hikurangi subduction zone, New Zealand. Science,
841 352(6286), 701-704.
842 Wallace, L. M., Kaneko, Y., Hreinsdóttir, S., Hamling, I., Peng, Z., Bartlow, N., ... & Fry, B.
843 (2017). Large-scale dynamic triggering of shallow slow slip enhanced by overlying
844 sedimentary wedge. Nature Geoscience, 10(10), 765-770.
845 Wallace, L. M., Saffer, D. M., Barnes, P. M., Pecher, I. A., Petronotis, K. E., & LeVay, L. J.
846 (2019). Hikurangi subduction margin coring, logging, and observatories. Proceedings of the
847 International Ocean Discovery Program, 372.
848 Wallace, L. M. (2020). Slow slip events in New Zealand. Annual Review of Earth and Planetary
849 Sciences, 48, 175-203.
850 Xing, T., Zhu, W., French, M., & Belzer, B. (2019). Stabilizing effect of high pore fluid pressure
851 on slip behaviors of gouge-bearing faults. Journal of Geophysical Research: Solid Earth,
852 124(9), 9526-9545.
853 Yasuhara, H., Marone, C., & Elsworth, D. (2005). Fault zone restrengthening and frictional
854 healing: The role of pressure solution. Journal of Geophysical Research: Solid Earth,
855 110(B6).

Figure 1.

A. Map of the Hikurangi subduction zone

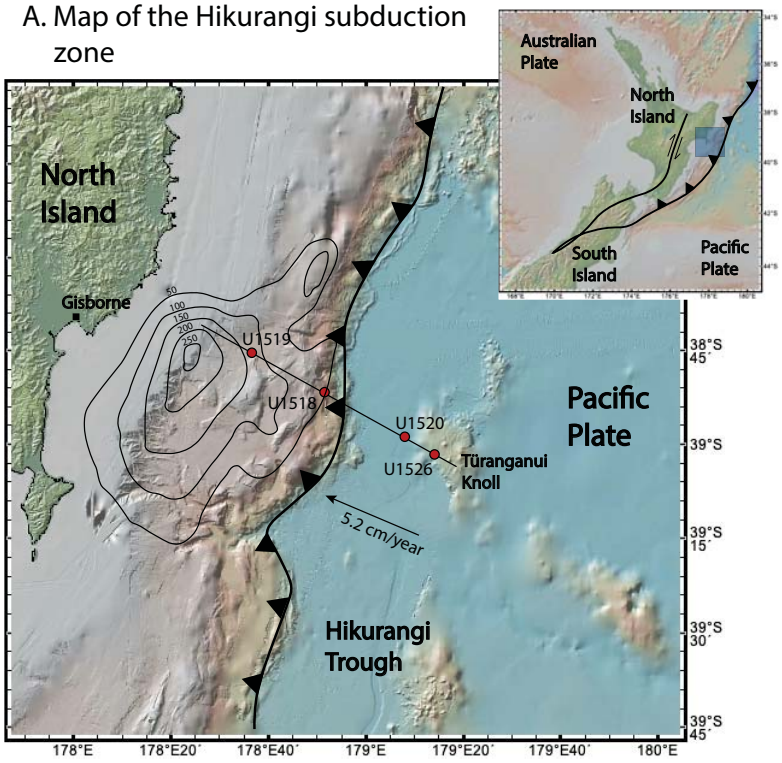

B. Reflection seismic profile of the subdution zone (05CM-04 line)

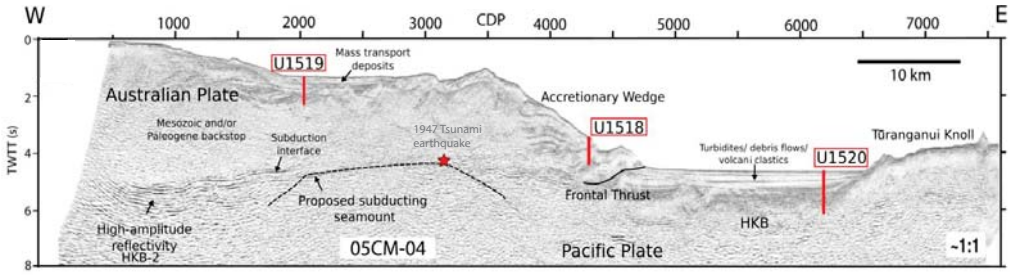

Figure 2.

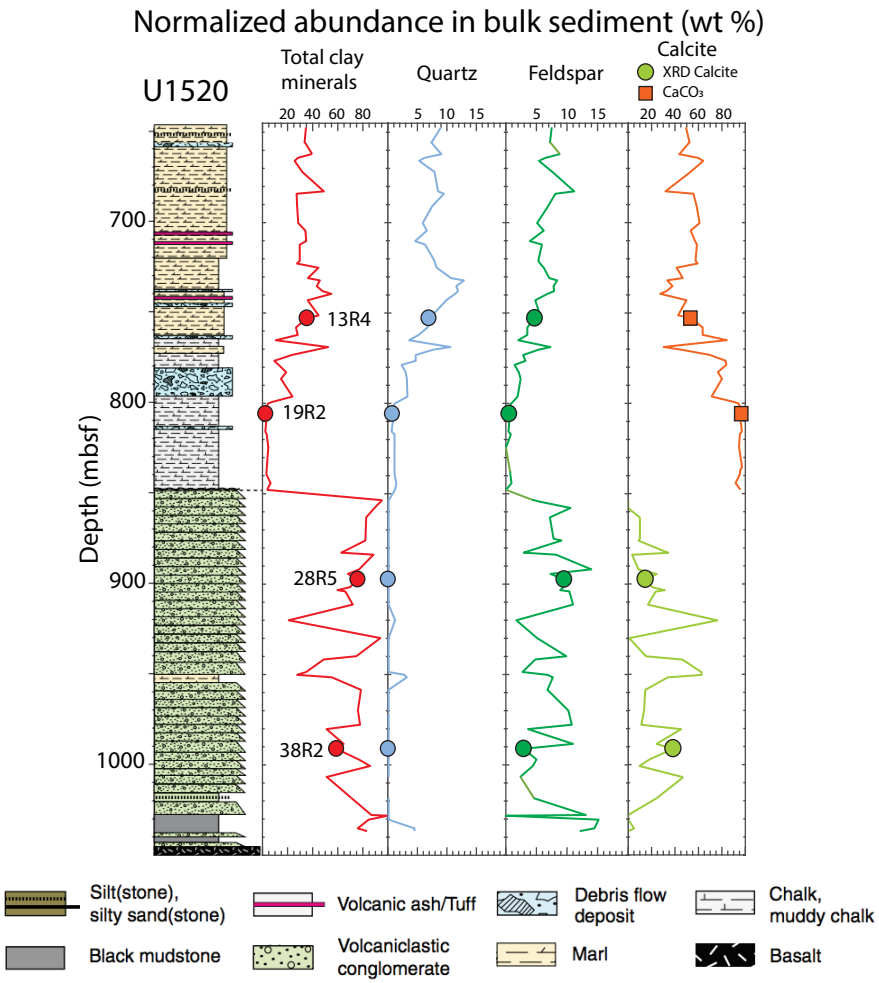
Normalized abundance in bulk sediment (wt %)
U1520
Total clay minerals
Quartz
Feldspar
Calcite
XRD Calcite
CaCO3
20 40 60 80
5 10 15
5 10 15
20 40 60 80
Depth (mbsf)
700
800
900
1000
13R4
19R2
28R5
38R2
Silt(stone), silty sand(stone)
Black mudstone
Volcanic ash/Tuff
Volcaniclastic conglomerate
Debris flow deposit
Marl
Chalk, muddy chalk
Basalt

Figure 3.

A Biaxial apparatus

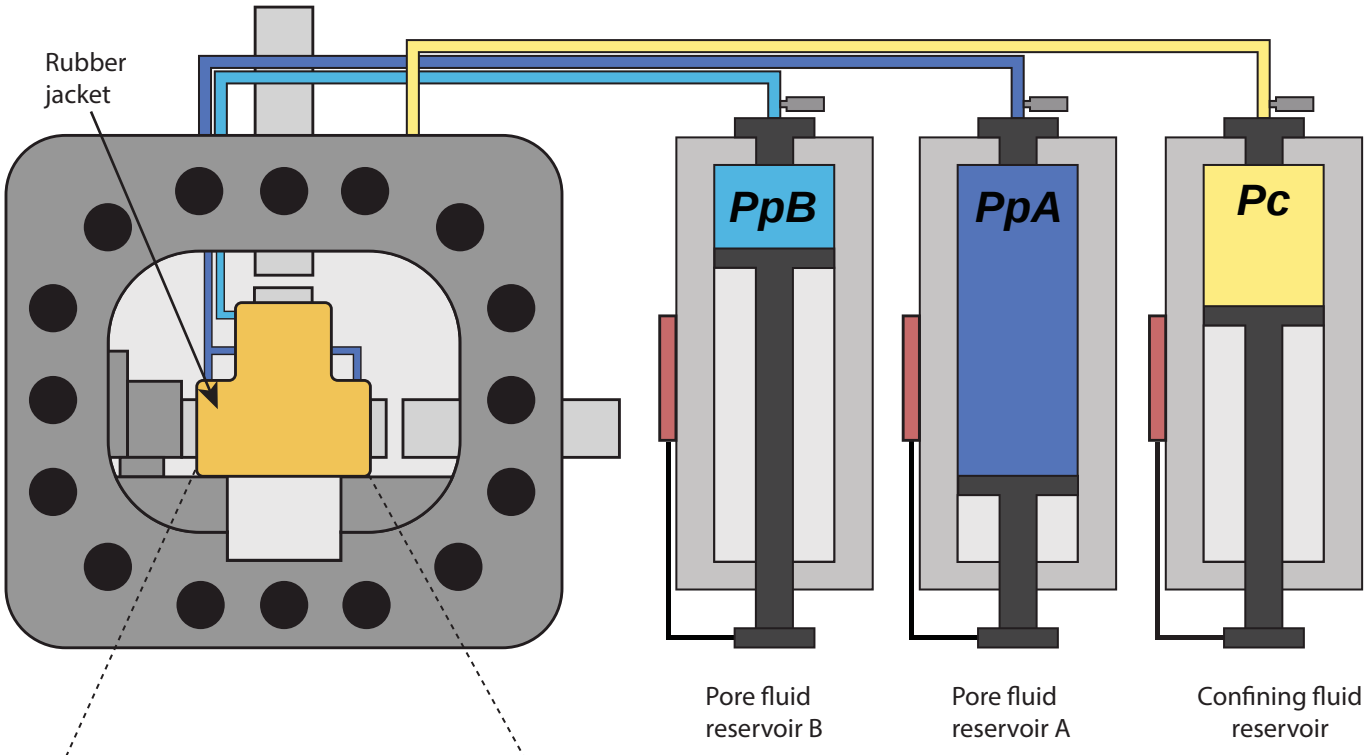

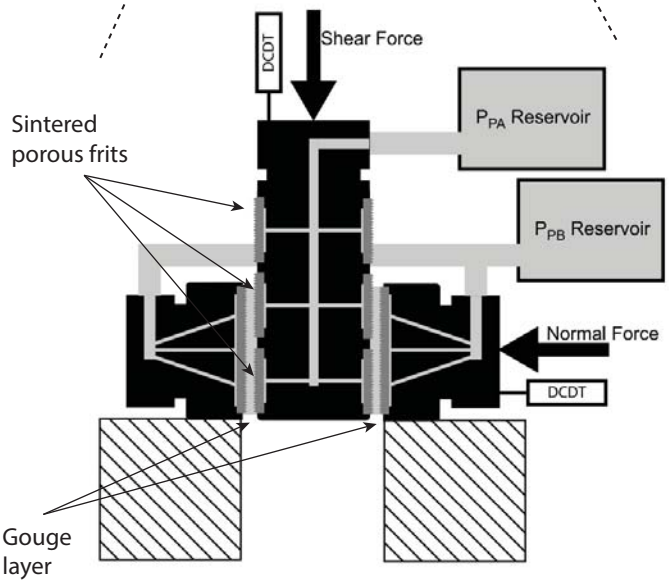

B Plate-rate apparatus

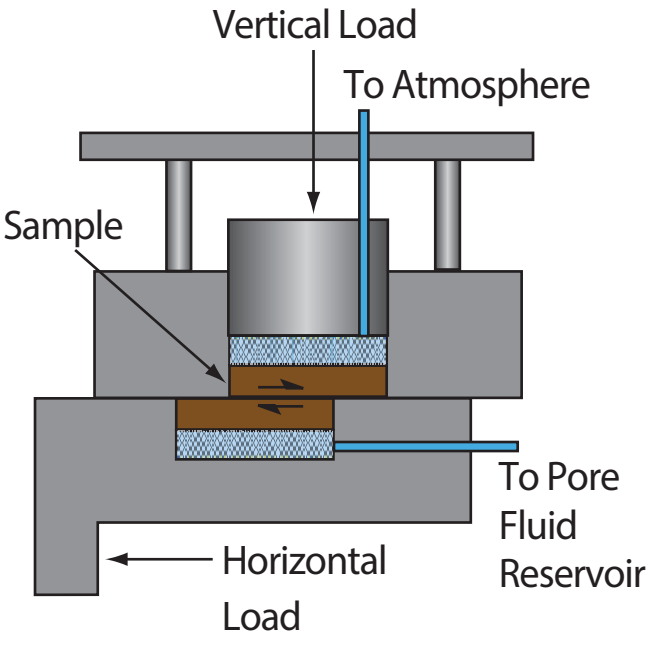

Figure 4.

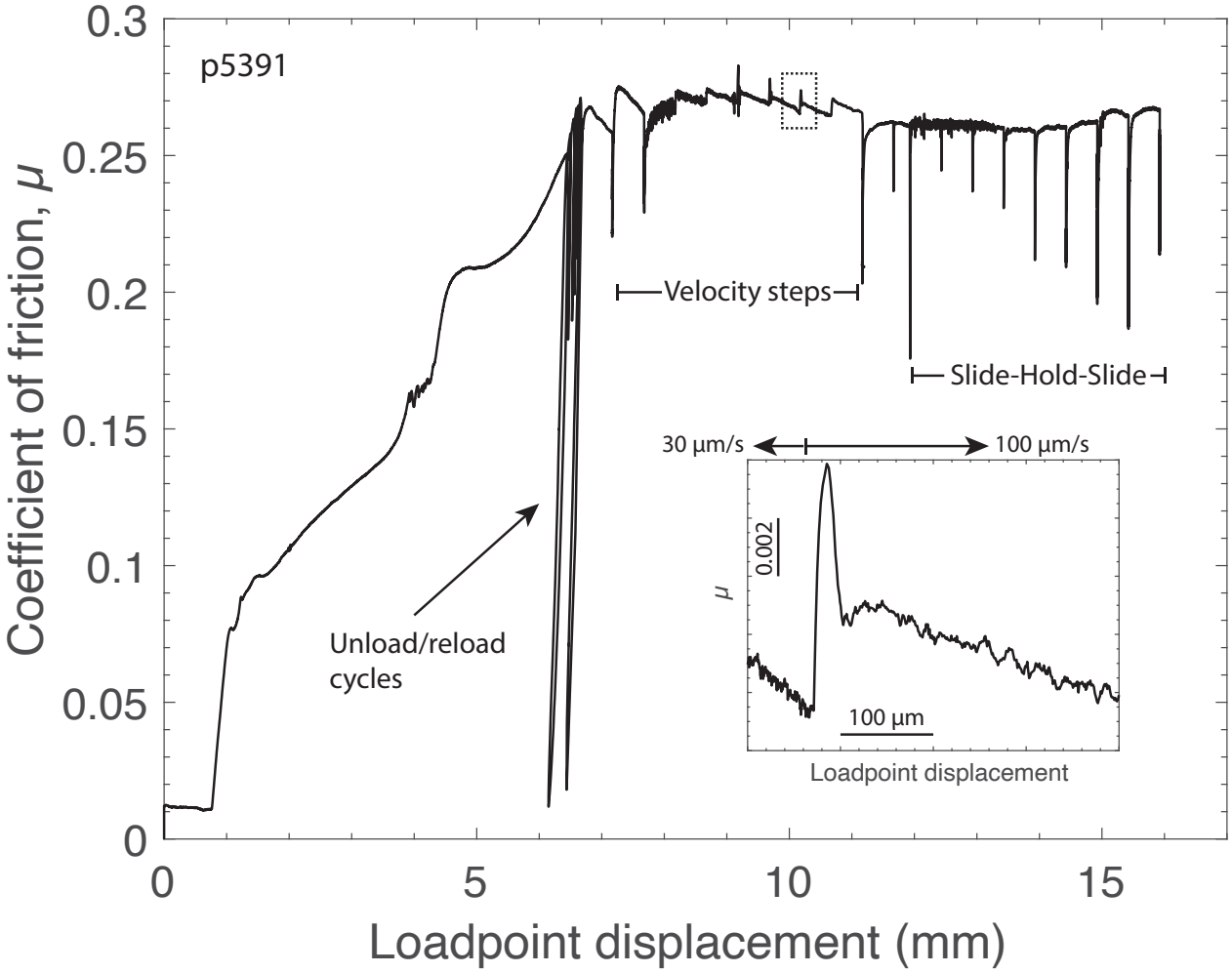
p5391
Coefficient of friction, μ
0.3
0.25
0.2
0.15
0.1
0.05
0
0
5
10
15
Loadpoint displacement (mm)
Velocity steps
Slide-Hold-Slide
Unload/reload
cycles
30 μm/s
100 μm/s
0.002
μ
100 μm
Loadpoint displacement

Figure 5.

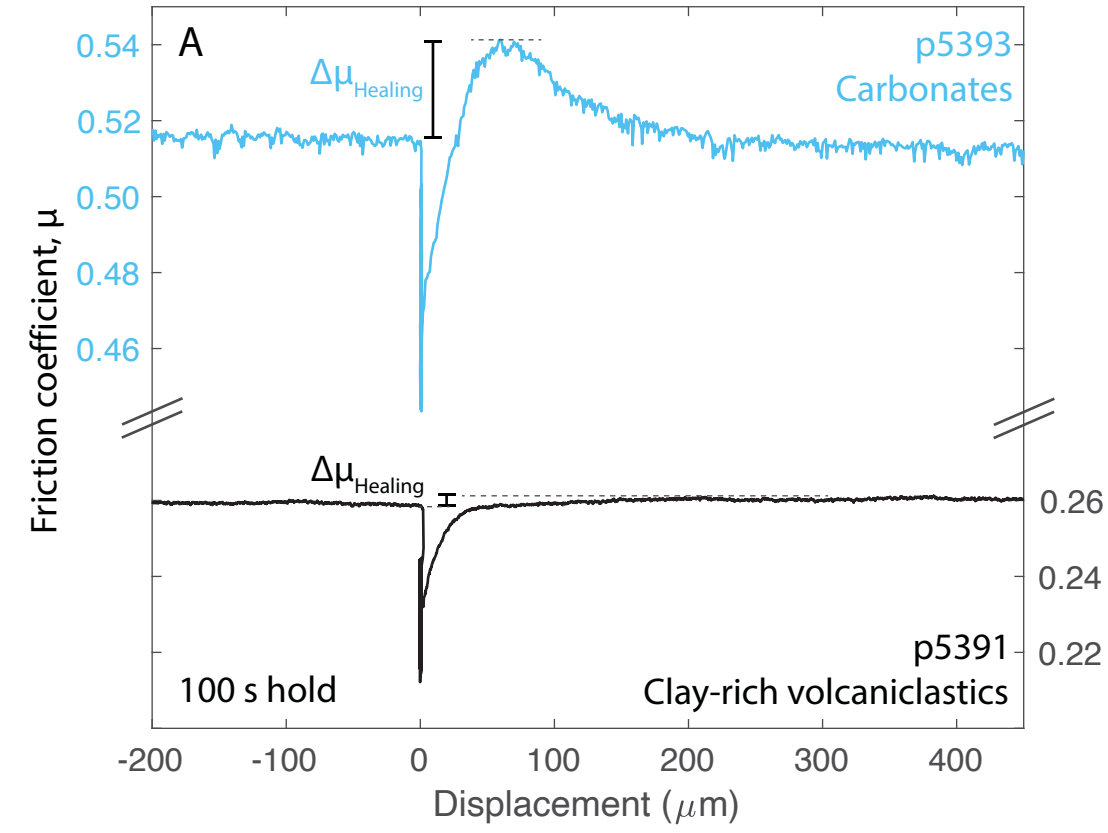
A
p5393
Carbonates
Δμ Healing
0.54
0.52
0.50
0.48
0.46
Friction coefficient, μ
Δμ Healing
0.26
0.24
0.22
p5391
Clay-rich volcaniclastics
100 s hold
-200
-100
0
100
200
300
400
Displacement (μm)

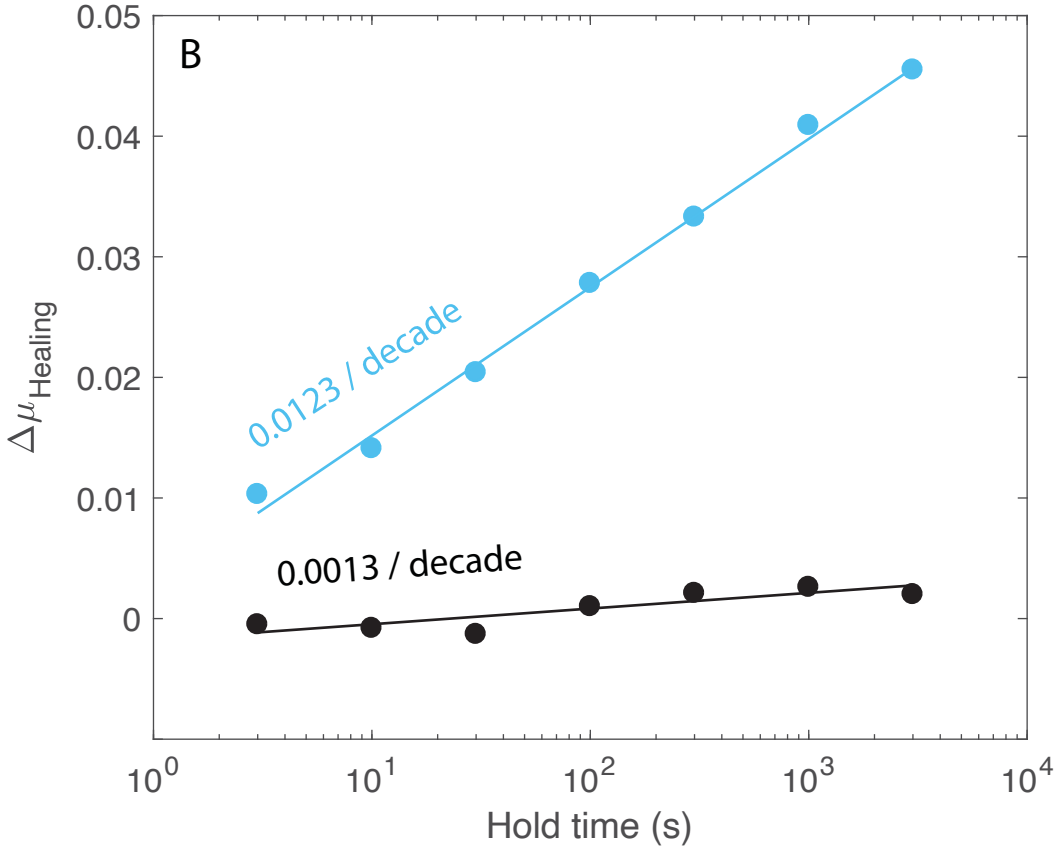
B
0.05
0.04
0.03
0.02
0.01
0
Δμ Healing
0.0123 / decade
0.0013 / decade
10^0
10^1
10^2
10^3
10^4
Hold time (s)

Figure 6.

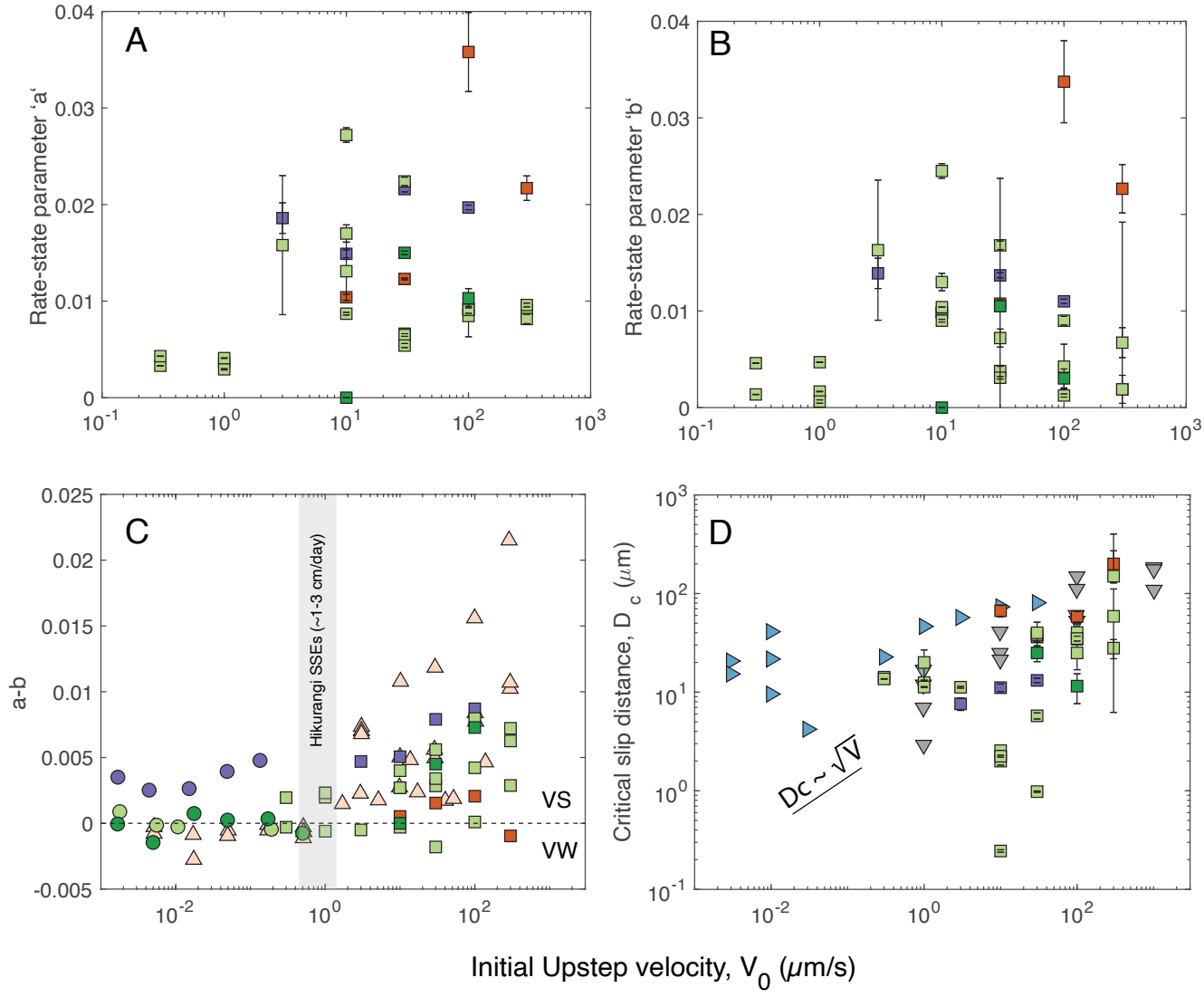

Legend (This study)

- Marl (U1520 13R)
- Carbonate (U1520 19R)
- Volcaniclastics (U1520 28R)
- Volcaniclastics (U1520 38R)
- Biax (double-direct shear)
- Plate-rate (single-direct shear)

- Rabinowitz et al. (2018)
- Mair and Marone (1999)
- Ikari et al. (2020b)

Figure 7.

U1520 28R5 Clay-rich volcaniclastic conglomerates (σ_{eff} = 25 MPa)

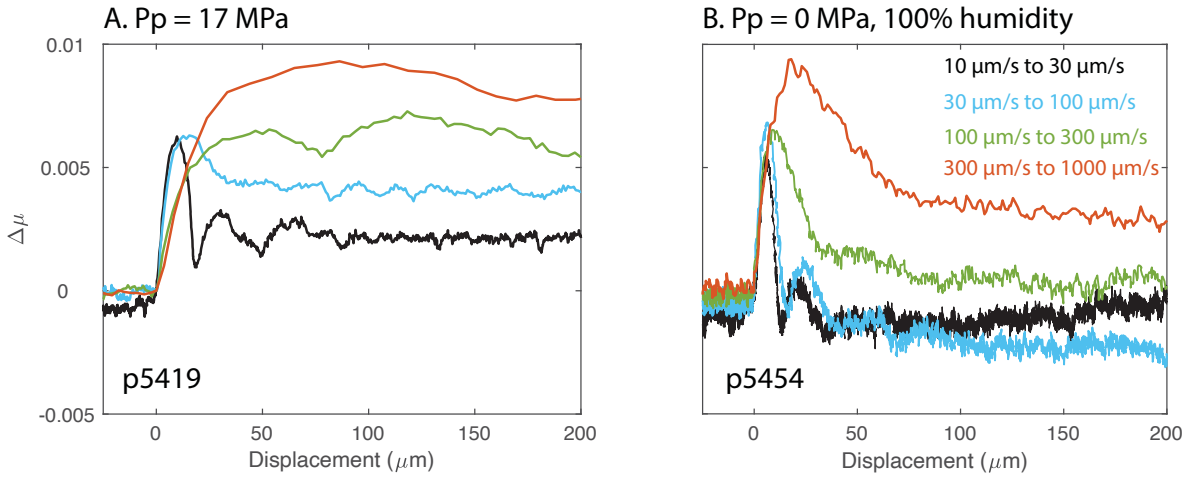

C

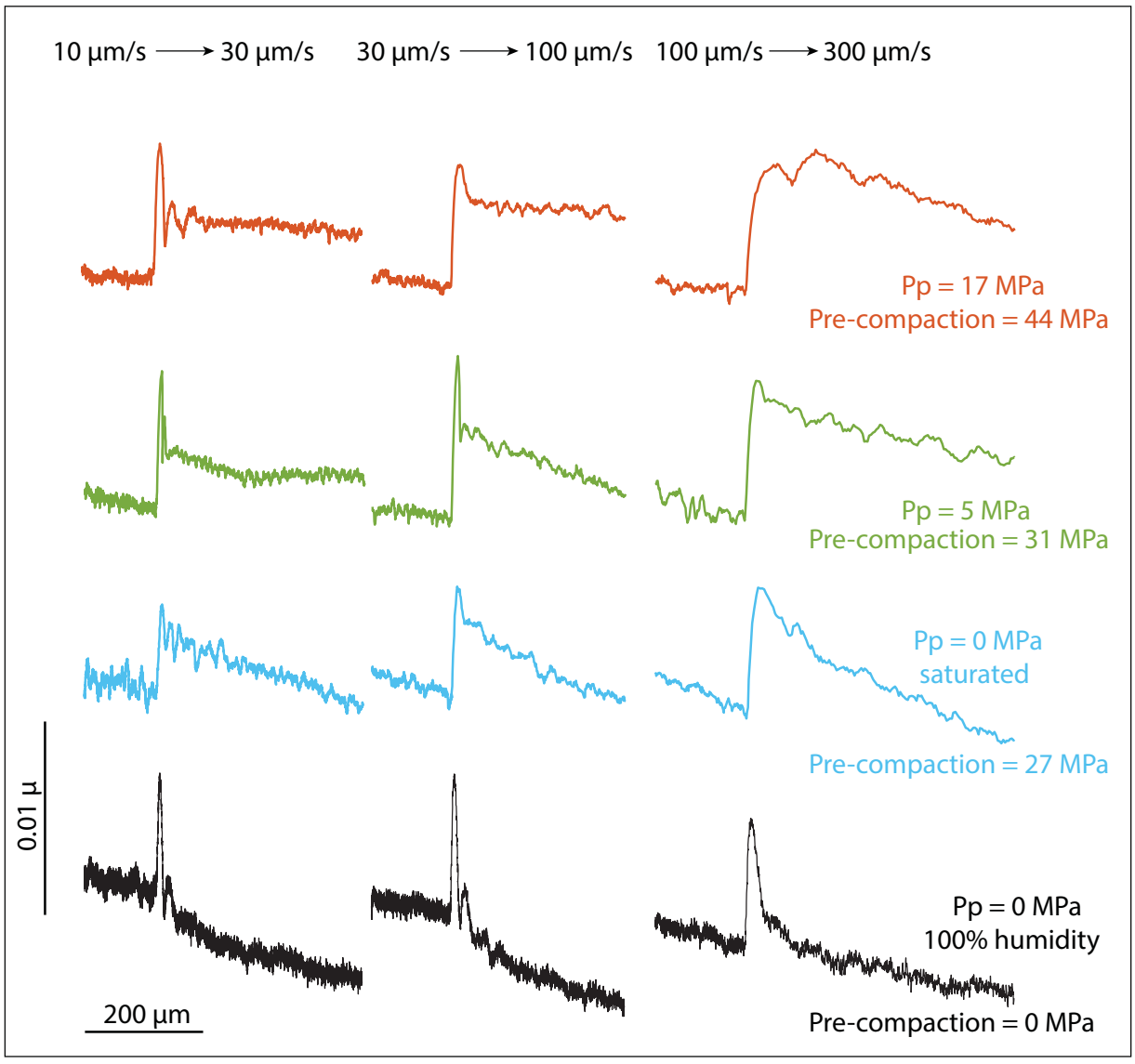

Figure 8.

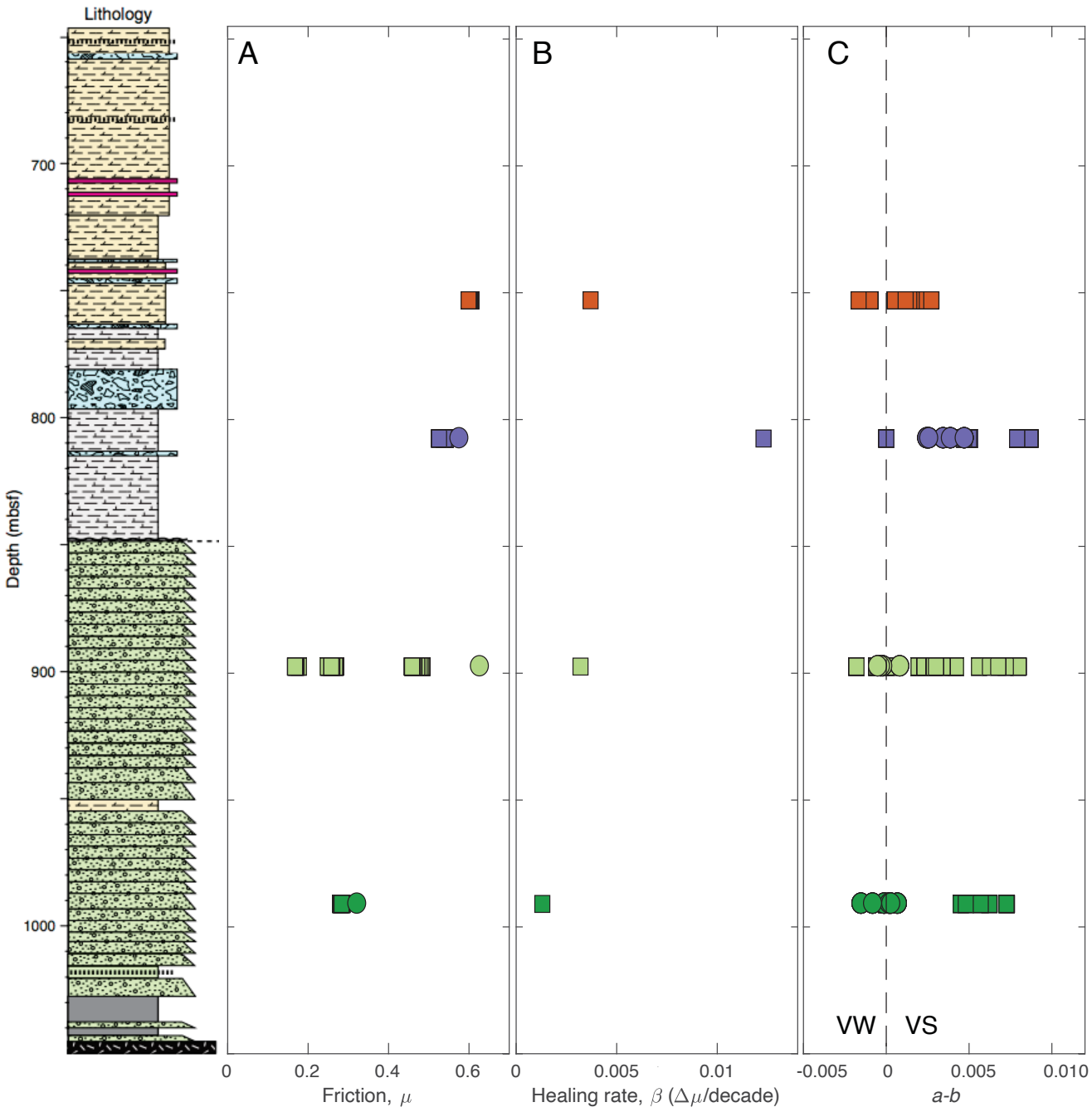

Legend

Marl (U1520 13R)

Carbonate (U1520 19R)

Volcaniclastics (U1520 28R)

Volcaniclastics (U1520 38R)

Biax (double-direct shear)

Plate-rate (single-direct shear)

Figure 9.

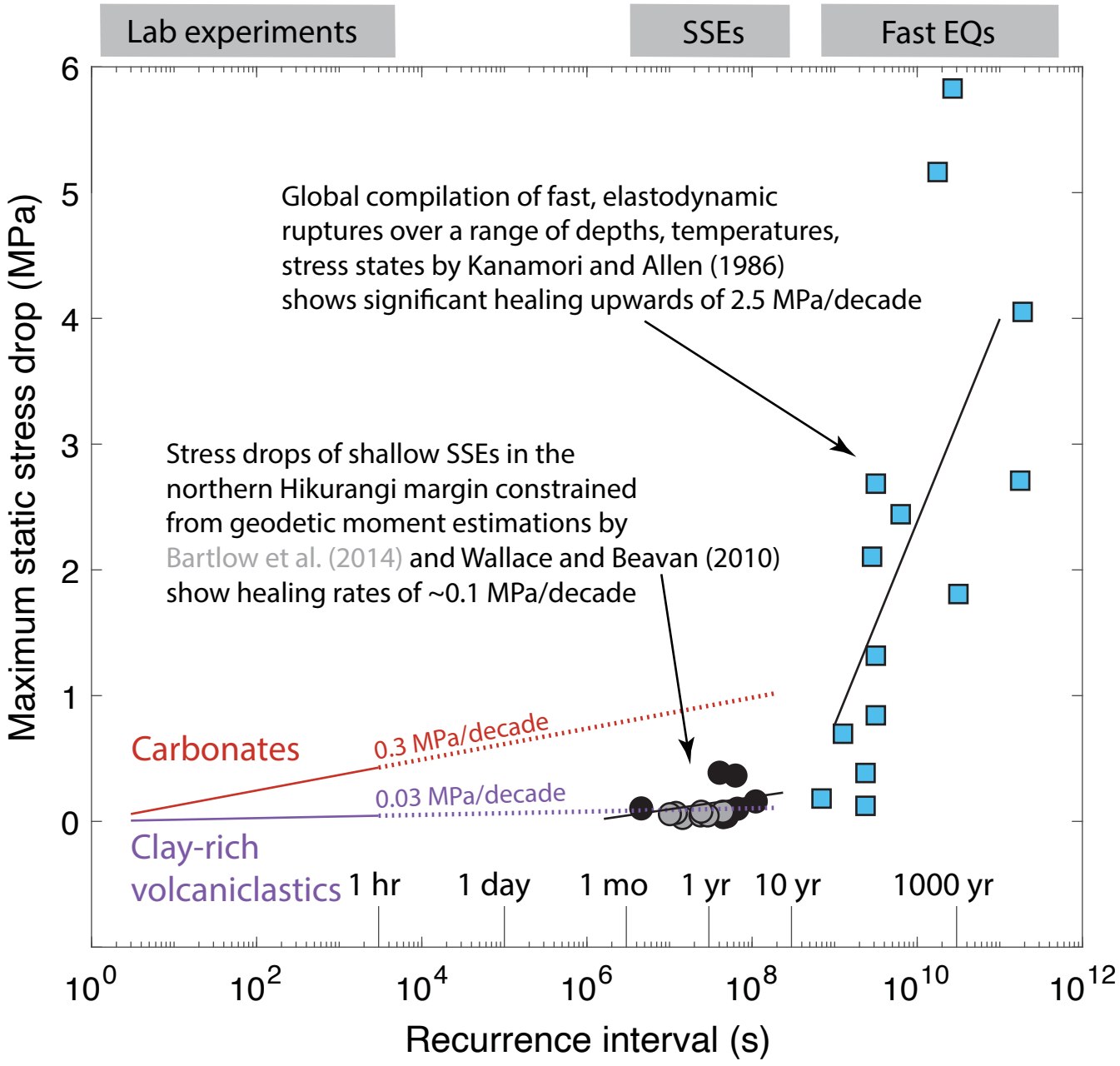
Lab experiments
SSEs
Fast EQs
Maximum static stress drop (MPa)
Recurrence interval (s)
Global compilation of fast, elastodynamic ruptures over a range of depths, temperatures, stress states by Kanamori and Allen (1986) shows significant healing upwards of 2.5 MPa/decade
Stress drops of shallow SSEs in the northern Hikurangi margin constrained from geodetic moment estimations by Bartlow et al. (2014) and Wallace and Beavan (2010) show healing rates of ~0.1 MPa/decade
Carbonates
0.3 MPa/decade
0.03 MPa/decade
Clay-rich volcaniclastics
1 hr
1 day
1 mo
1 yr
10 yr
1000 yr

Figure 10.

Conditionally stable
clay-rich volcaniclastic matrix
May nucleate and host shallow SSE
due to low frictional healing and
velocity-dependent RSF parameters.

Accretionary wedge

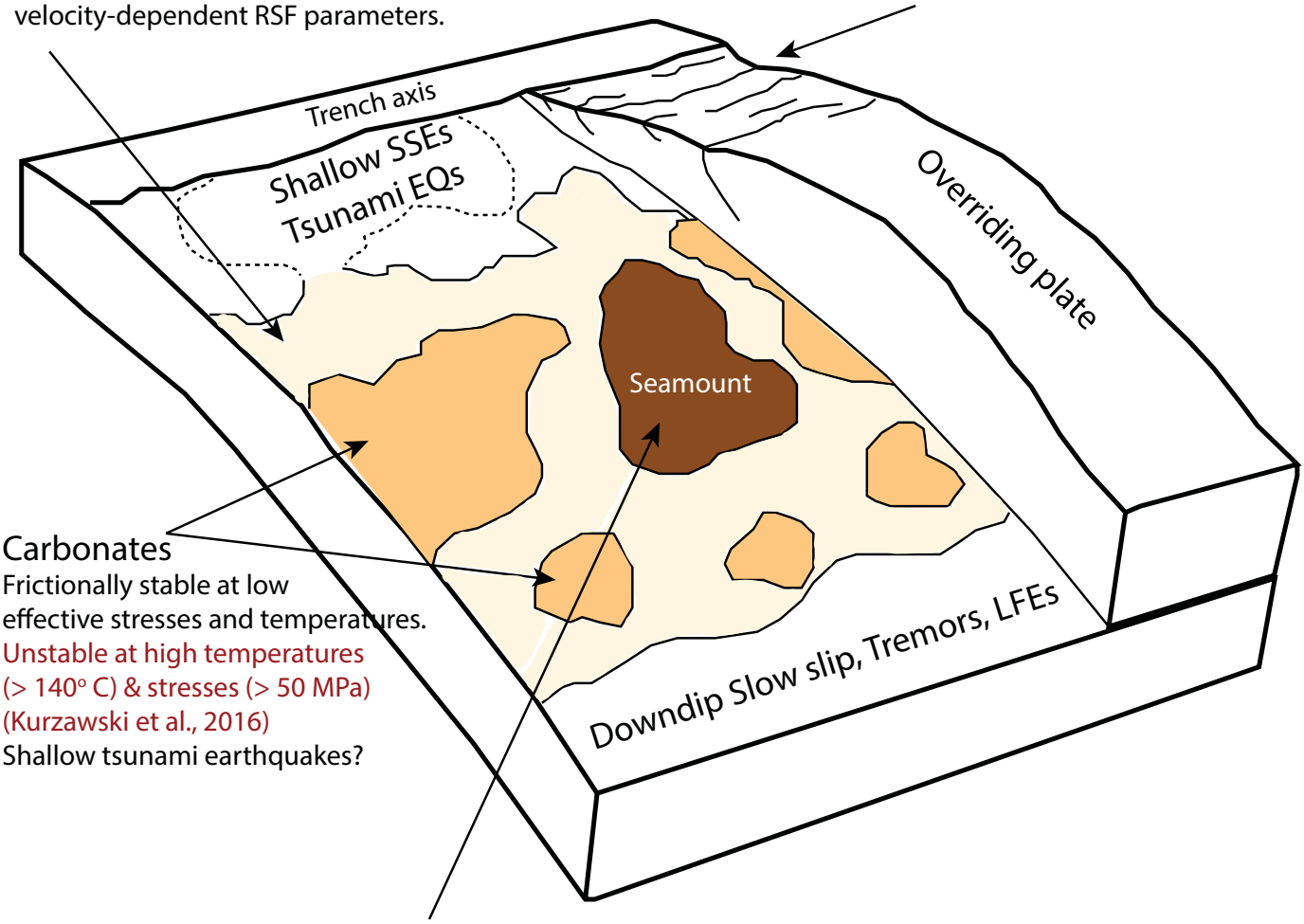

Carbonates
Frictionally stable at low
effective stresses and temperatures.
Unstable at high temperatures
(> 140° C) & stresses (> 50 MPa)
(Kurzawski et al., 2016)
Shallow tsunami earthquakes?

Basaltic seamounts
Weakly velocity-neutral and
(a-b) independent of
velocity (Ikari et al., 2020c)
Shallow SSE nucleation?